XI. PLASMA ELECTRONICS*

Prof. L. D. Smullin
Prof. H. A. Haus
Prof. A. Bers
Prof. W. D. Getty
Prof. D. J. Rose
Prof. T. H. Dupree
Prof. L. M. Lidsky
Prof. E. P. Gyftopoulos
Dr. T. Musha
R. R. Bartsch
T. S. Brown
J. F. Clarke
J. A. Davis
F. E. Dunn
P. H. Edmonds
S. A. Evans
T. J. Fessenden
R. W. Flynn
F. Gardiol
E. T. Gerry
J. N. Hamawi
C-F. G. Hsi
G. I. Kachen, Jr.
C. A. Kapentanakos
B. R. Kusse
S. H. Kyong
M. A. Lieberman
M. Lind
M. D. Lubin
J. D. Mills
R. W. Moir
A. A. Offenberger
K. C. Papadopoulos
R. R. Parker
L. M. Petrie, Jr.
C. S. Ribbeck
H. M. Schneider
E. Thompson
C. E. Wagner
R. N. Wallace
J. C. Woo

A. ION-PLASMA OSCILLATIONS

The plasma density of the electron-cyclotron resonance discharge (ECRD) has been measured with an 8-mm Fabry-Perot microwave interferometer. The ECRD experiment has been described in Quarterly Progress Report No. 73 (pages 81-85) and Quarterly Progress Report No. 75 (pages 120-121). The discharge is driven by a 2.4-Gc, 1.2-kw magnetron, powered by an unfiltered 5-kv power supply. The magnetron current and voltage waveforms are shown in Fig. XI-1.

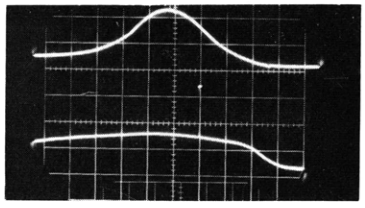

Fig. XI-1. Magnetron current and voltage vs time. Upper trace: magnetron current, 0.1 amp/cm. Lower trace: magnetron voltage, 5000 volts/cm. Time scale, 0.5 msec/cm.

The Fabry-Perot interferometer has been described in Quarterly Progress Report No. 76 (pages 109-111). It consists of a pair of spherical copper mirrors mounted facing each other in the side wall of the discharge tube. The mirrors are $3\frac{1}{2}$ inches in diameter and approximately 6 inches apart. The mirror system is confocal, that is, each mirror is focused at the center of the discharge tube. A 35-Gc, 10-mw klystron provides the power for this system. The microwave energy is fed from the 8-mm waveguide into

*This work was supported in part by the National Science Foundation (Grant GK-57).

and out of the resonating system through a small hole in the center of each mirror. A crystal is used to detect the microwave energy passing through the resonating system.

The klystron is modulated by a sawtooth whose period τ_s is short compared with the width of the magnetron current pulse. Typically, τ_s is approximately 3.5 μsec. As the klystron is swept in frequency, a fringe or "pip" is detected and displayed on an oscilloscope when the klystron frequency coincides with a resonant frequency of the mirror system. As the plasma builds up inside the discharge tube, the position of this fringe shifts. By measuring this shift, the electron density of the plasma may be determined.

The interferometer phase shift as a function of time has been measured for various values of the pressure and magnetic field in a hydrogen discharge. The electron density was then calculated, under the assumption that the plasma uniformly filled the discharge tube. The actual density profile in the discharge tube has not yet been determined. In Fig. XI-2, a typical plot of the electron density against time is shown. Each point on the plot represents a separate magnetron current pulse. This pulse is shown in Fig. XI-2 as a dotted line. Even though the shape and height of the magnetron current do not vary from pulse to pulse, the pulse-to-pulse variation of the plasma density at any time within a magnetron current pulse is considerable. This indicates that the plasma density is

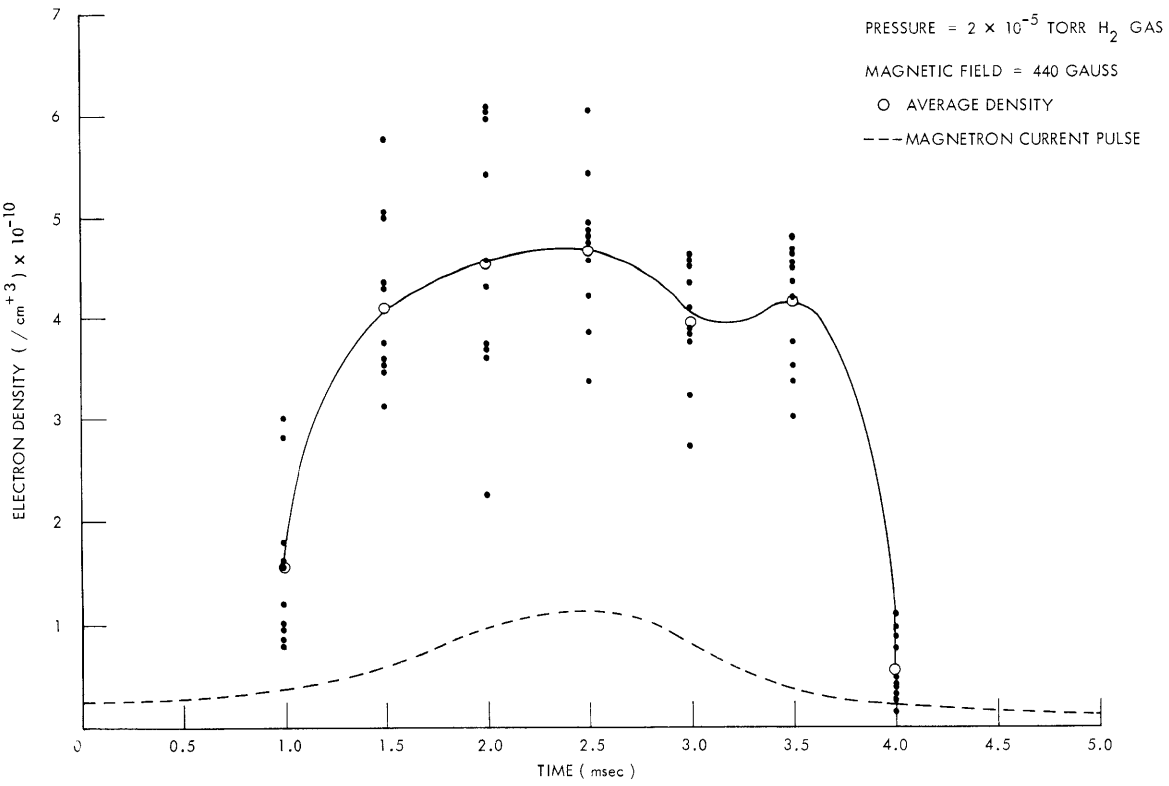

Fig. XI-2. Electron density vs time in ECRD.

fluctuating considerably (by 50 per cent or more) in the ECRD, and on a time scale that is long compared with τ_s, the interferometer sweep time. The fluctuation frequency is thus bounded above by $\frac{1}{\tau_s} \approx 30$ kcps and below (presumably) by 60 cps.

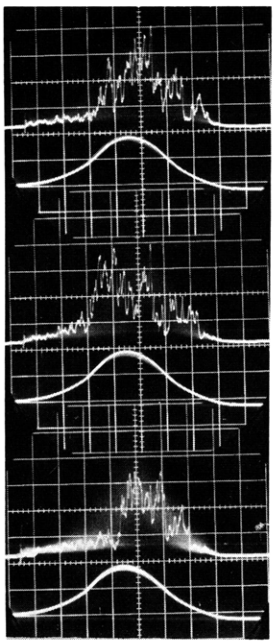

Fig. XI-3. Retarding potential probe plate current vs time ($p = 4 \times 10^{-6}$ torr Hg, $B_o = 400$ gauss). Upper trace: retarding potential probe plate current. Lower trace: magnetron current pulse. Time scale 0.5 msec/cm.

In order to examine the fluctuating plasma in more detail, the current reaching the plate of a retarding potential probe was measured as a function of time. The retarding potential probe is mounted on the axis of the discharge tube just back of the magnetic mirror. The probe consists of a capped copper tube, $\frac{3}{4}$ inch in diameter and approximately 2 inches long. A hole of 25-mil diameter has been drilled in the cap to sample the plasma. Behind the cap are arranged three grids and a plate. In this experiment, the grids were all grounded and the plate is held at +180 volts.

Figure XI-3 shows three separate magnetron current pulses and the corresponding plate current of the retarding potential probe. For these three pulses, the magnetic field in the center of the discharge tube was 440 gauss and the pressure was 4×10^{-6} torr. The fluctuations in the plate current provide a strong indication that the plasma density itself is fluctuating.

The fluctuating frequency can be estimated from Fig. XI-3 to be approximately 6000 cps.

In Fig. XI-4 the average density of the plasma at peak magnetron current (2.5 msec) has been plotted against the magnetic field in the center of the discharge tube, with pressure as a parameter. Note that the magnetic-mirror ratio for this experiment is approximately 4. The lower dotted line is the electron

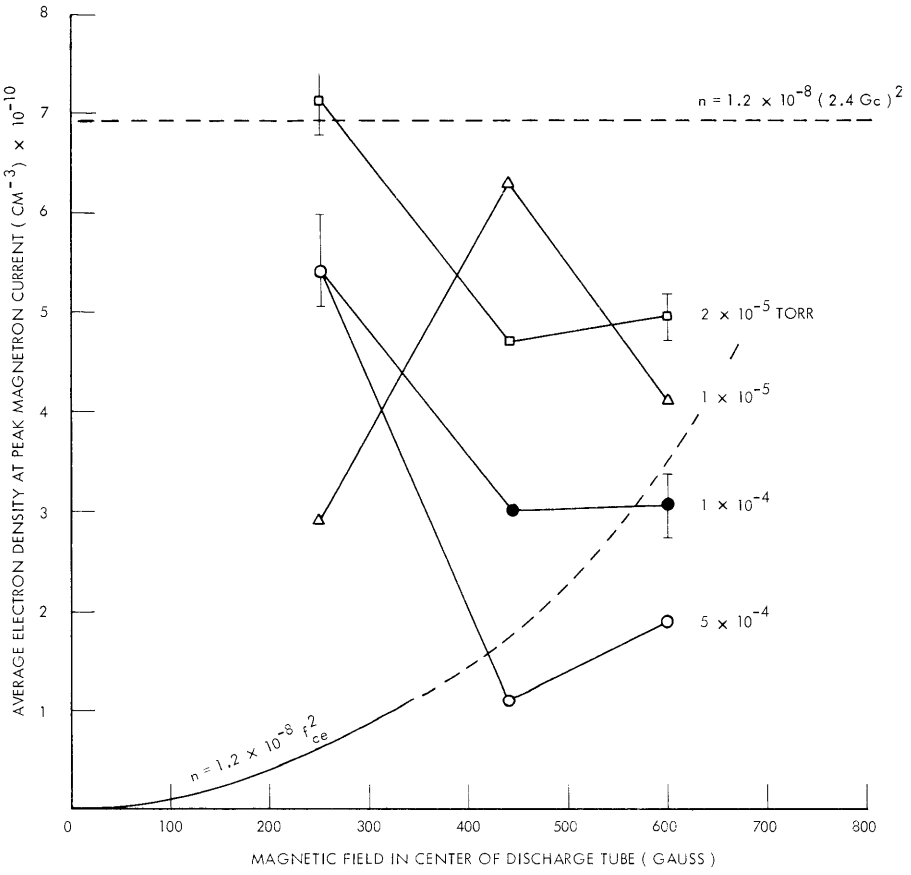

Fig. XI-4. Average electron density vs magnetic field.

density found by assuming that the electron cyclotron and electron plasma frequencies are equal at the center of the discharge tube. The upper dotted line gives the density corresponding to a plasma frequency of 2.4 Gc, the driving frequency of the magnetron. It appears that the average electron density is limited by the magnetron frequency (upper dotted line). Several more points must be taken, however, to complete Fig. XI-4.

M. A. Lieberman

B. DISPERSION DIAGRAMS FOR HOT-ELECTRON PLASMAS

1. Computer Program for Solving Transcendental Dispersion Equations

A computer program has been written to find the zeros of a transcendental dispersion function $\underline{D}(\underline{\omega}, k, \ldots)$ in the complex $\underline{\omega}$ plane. This program must be used in conjunction with the Project MAC time-sharing system.

The user must provide a subroutine that computes the value of $\underline{D}$, given the complex frequency $\underline{\omega}$, wave number k and any other parameters that the user may desire. The subroutine may be written by using MAD, FORTRAN or FAP programming languages.

In operation, the program continuously steps k by an increment Δk, and at each step finds a zero, $\underline{\omega}_n$, of the dispersion function $\underline{D}$

$$\underline{D}(\underline{\omega}_n, k+n\Delta k, \ldots) = 0.$$

The zero, $\underline{\omega}_n$, is found by constructing a grid of values in the complex ω plane around an initial guess ω_{gn} as follows:

$$\begin{cases} \underline{\omega}_{go} = \text{provided by the user} \\ \underline{\omega}_{g1} = \underline{\omega}_o \\ \omega_{gn} = \underline{\omega}_{n-1} + \Delta k(\underline{\omega}_{n-1} - \underline{\omega}_{n-2}) \qquad n \geq 2. \end{cases}$$

The program evaluates the real function $F = |D(\underline{\omega}, k+n\Delta k, \ldots)|^2$ for every point on the grid. If a minimum of F is found at ω_n, the grid is refined several times until $\underline{\omega}_n$ is given to three significant figures; then $\underline{D}$ is checked to verify that its real and imaginary parts change sign in the neighborhood of $\underline{\omega}_n$. If such is the case, the zero is printed and k is stepped. Thus the zeros of D in the complex $\underline{\omega}$ plane are computed as a function of the wave number k.

Man-machine interaction plays an important role in the use of this program. It would be practically impossible to utilize this program in an efficient manner without the aid of the time-sharing system. The grid size and spacing in the complex $\underline{\omega}$ plane, the wave number k and its increment Δk, and all other parameters are specified by the user and may be altered at will. If at any step a zero of $\underline{D}$ is not found, the program requests the user to change the grid size, spacing, and location in the complex $\underline{\omega}$ plane. As an aid to the user, the program will print the values of $\underline{D}$ and F at the grid points if desired.

2. Longitudinal Waves in the Absence of a Magnetic Field

The dispersion equation for longitudinal waves propagating in a hot-electron Maxwellian plasma[1] is

$$1 + \frac{1}{k^2\lambda_D^2}\left[1 + \frac{1}{\sqrt{2}\,k\lambda_D}\frac{\omega}{\omega_{pe}} Z\left(\frac{1}{\sqrt{2}\,k\lambda_D}\frac{\omega}{\omega_{pe}}\right)\right] = 0,$$

where ω_{pe} is the electron plasma frequency, $\lambda_D = \frac{V_T}{\omega_{pe}}$ is the Debye wavelength, and

$$Z(\xi) = \pi^{-1/2}\int_{-\infty}^{\infty} dx\,\frac{e^{-x^2}}{x-\xi} \qquad \text{Im } \xi > 0$$

is the plasma dispersion function, tabulated by Fried and Conte.[2]

The solution of this dispersion equation is shown in Fig. XI-5. The familiar Landau damping result is obtained for $k\lambda_D \ll 1$, while for $k\lambda_D$ much in excess of 1, the wave is heavily damped.

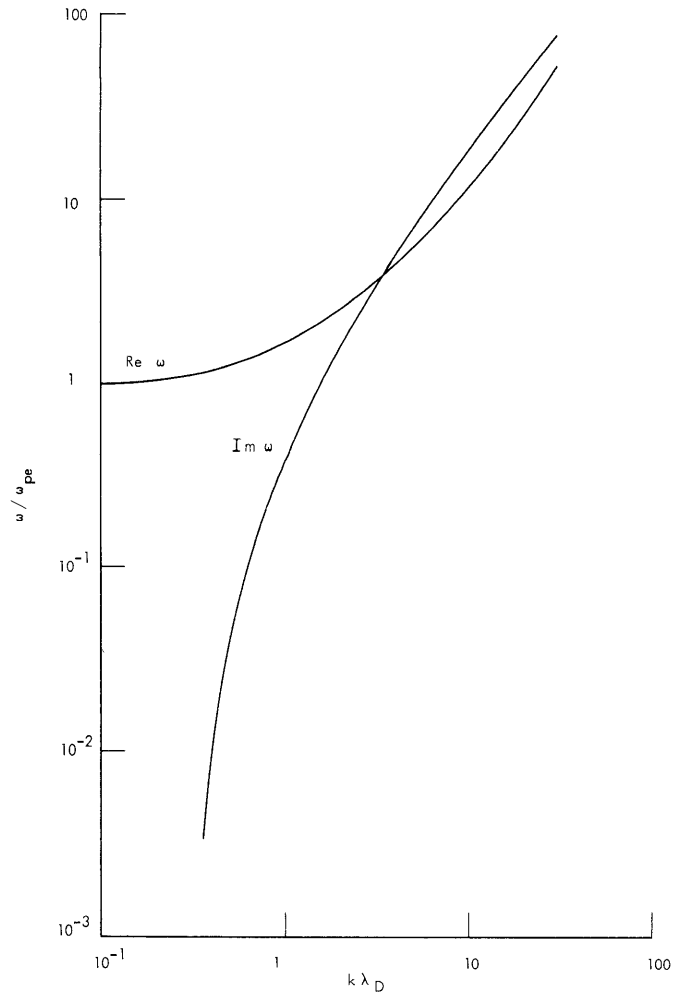

Fig. XI-5. Plasma dispersion equation for longitudinal waves.

3. Quasi-static Waves in a Hot-Electron Plasma Waveguide

Consider a hot-electron plasma waveguide whose axis is parallel to the static magnetic field. Under the assumption that as a boundary condition the tangential electric

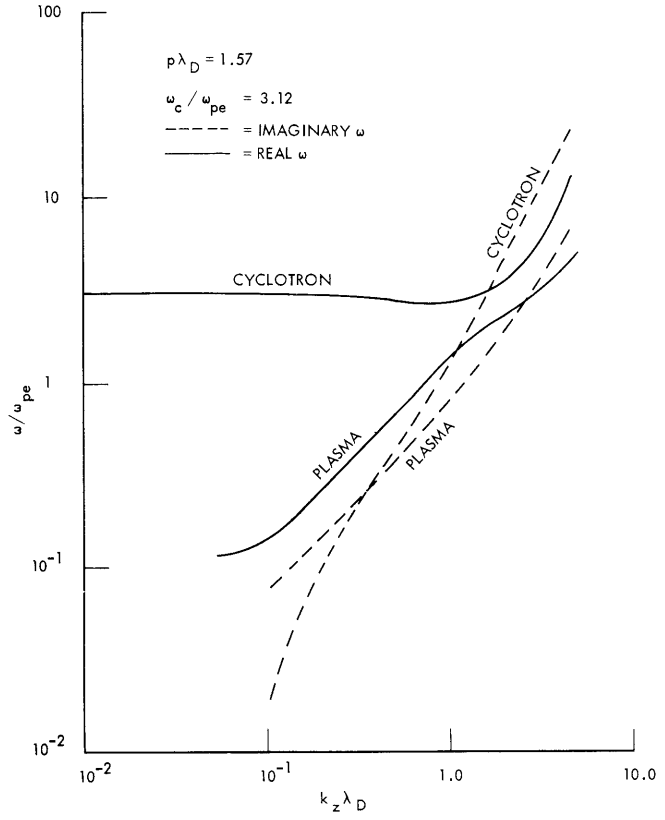

Fig. XI-6. Quasi-static dispersion equation in a hot-electron plasma waveguide.

field vanishes at the waveguide walls, the quasi-static dispersion equation for this system[1] is

$$1 + \frac{1}{\left(k_z^2+p^2\right)\lambda_D^2}\left[1 + \xi_o \sum_{n=-\infty}^{\infty} Z(\xi_n)\, I_n(\lambda)\, e^{-\lambda}\right] = 0,$$

where $\xi_n = \left(\frac{1}{\sqrt{2}\,k_z\lambda_D}\right)\left(\frac{\omega}{\omega_{pe}} - n\frac{\omega_c}{\omega_{pe}}\right)$, $\lambda = p\lambda_D \Big/ \left(\frac{\omega_c}{\omega_{pe}}\right)$, ω_c is the electron cyclotron frequency, k_z is the longitudinal wave number, p is the transverse wave number, and $I_n(x)$ is the Bessel function of imaginary argument.

$$I_n(x) = i^{-n} J_n(ix).$$

This dispersion equation has an infinite number of solutions, each one corresponding roughly to a cyclotron frequency harmonic. For these solutions, $\omega \to n\omega_c$ as $k_z \to 0$. In addition to these waves, there is a single plasma wave, for which $\omega \to 0$ as $k_z \to 0$.

Through the use of the computer program described above the two solutions for the plasma wave and the first-harmonic cyclotron wave have been obtained. Figure XI-6 shows the solutions for the parameters $p\lambda_D = 1.57$, $\omega_c/\omega_{pe} = 3.12$. There is a crossover point at $k_z\lambda_D = 0.35$. Below this wave number, the cyclotron wave dominates the behavior of the waveguide system, since it has the smaller loss. Both waves are damped out for $k_z\lambda_D$ much greater than 2.5.

It should be noted that quasi statics is invalid in the neighborhood of the electron cyclotron frequency and its harmonics. Also, the question of boundary conditions arises. In a plasma with transverse, as well as longitudinal, temperature, plasma particles are constantly hitting the walls. It is not clear whether the boundary condition considered here, that the tangential electric field be zero on the waveguide wall, even approximates the actual plasma boundary condition.

M. A. Lieberman

References

1. T. Stix, The Theory of Plasma Waves (McGraw-Hill Publishing Company, New York, 1962), p. 103.

2. B. Fried and S. Conte, The Plasma Dispersion Function (Academic Press, New York, 1961).

C. INSTABILITIES IN ELECTRON STREAMS IN CROSSED ELECTRIC AND MAGNETIC FIELDS

We have been studying the properties of a hot, weak-density, unneutralized electron beam, whose unperturbed motion consists of a drift perpendicular to crossed static electric and magnetic fields.

In the unperturbed state, we assume that the average velocity of the electrons is given by $\bar{v}_{ave} = v_{0x}\bar{i}_x$, where $v_{0x} = E_0/B_0$. (See Fig. XI-7.) Here $E_0\bar{i}_y$ and $B_0\bar{i}_z$ are the applied, static electric and magnetic fields. We neglect the DC space charge and current, and the zero-order fields produced by them. The Boltzmann equation for this unperturbed state is satisfied by the distribution function

$$f_0 = A \exp\left[-\frac{1}{2} m \frac{(v_x - v_{0x})^2}{k_B T}\right] \exp\left[-\frac{1}{2}\frac{mv_y^2}{k_B T}\right] g(v_z), \tag{1}$$

where $v_{0x} = E_0/B_0$, A is a normalization constant, v_x, v_y, and v_z are the x, y, and

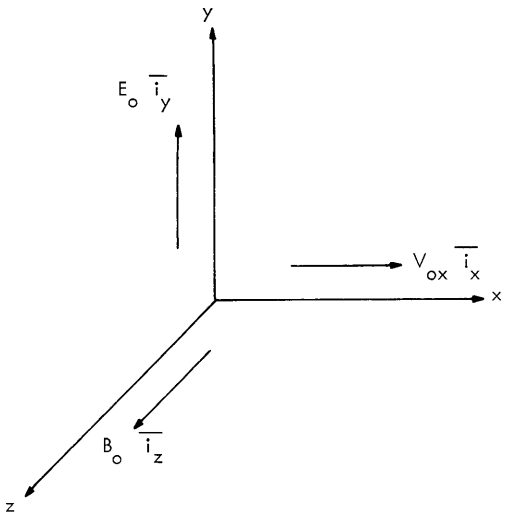

Fig. XI-7. Coordinate system for electron stream in crossed electric and magnetic fields.

z components of the particle velocity, m is the electron mass, T is the temperature, and k_B is Boltzmann's constant. The function $g(v_z)$ is left arbitrary at this point. Note that f_0 is spatially homogeneous and independent of time; it satisfies

$$\frac{q}{m}(E_0\bar{i}_y+\vec{v}\times B_0\bar{i}_z)\cdot\nabla_v f_0 = 0, \tag{2}$$

where q is the charge of a single electron.

If this unperturbed motion is given a perturbation so that the distribution function $f = f_0 + \mathrm{Re}\,[f_1 e^{j(\omega t-\bar{k}\cdot\bar{r})}]$, the linearized Boltzmann equation becomes

$$j(\omega-\bar{k}\cdot\bar{v})\,f_1 + \frac{q}{m}E_0\frac{\partial f_1}{\partial v_y} + \frac{q}{m}(\vec{v}\times B_0\bar{i}_z)\cdot\nabla_v f_1 = -\frac{q}{m}\bar{E}_1\cdot\nabla_v f_0. \tag{3}$$

Here $\bar{E}_1$ is the perturbed electric field. We shall make the quasi-static assumption, namely that the perturbed magnetic field $\bar{B}_1 = 0$, and hence $\bar{E}_1 = -\nabla\Phi$. Equation 3 is difficult to solve, however, owing to the term involving E_0.

If a Galilean transformation is made to a coordinate system translating with the average velocity $v_{0x}\bar{i}_x$ of the electrons, the static electric field vanishes and the problem is considerably simplified. This transformation may be described by the relations

$$\vec{r} = \vec{r'} + v_{0x}\bar{i}_x t \tag{4}$$

$$\vec{v} = \vec{v'} + v_{0x}\bar{i}_x \tag{5}$$

$$t = t' \tag{6}$$

$$\bar{E} = \bar{E}' - v_{0x}\bar{i}_x \times \bar{B}' \tag{7}$$

$$\bar{B} = \bar{B}'. \tag{8}$$

The symbol prime denotes quantities measured in the moving system, while unprimed quantities are measured in the laboratory system. In Eqs. 4-8, we have assumed $\frac{v_{0x}}{c} \ll 1$, where c is the velocity of light. In the moving coordinate system, the Boltzmann equation becomes

$$\frac{\partial f(\bar{r}', \bar{v}', t')}{\partial t'} + \bar{v}' \cdot \nabla_{r'} f(\bar{r}', \bar{v}', t') + \frac{q}{m}\left[\bar{E}' + \bar{v}' \times B'\right] \cdot \nabla_{v'} f(\bar{r}', v', t',) = 0. \tag{9}$$

The unperturbed distribution function is

$$f = A \exp\left[-\frac{1}{2}\frac{mv_x'^2}{k_B T}\right] \exp\left[-\frac{1}{2}\frac{mv_y'^2}{k_B T}\right] g(v_z') \tag{10}$$

which satisfies the unperturbed Boltzmann equation

$$\frac{q}{m}(\vec{v}' \times B_0 \bar{i}_z) \cdot \nabla_{v'} f_0 = 0. \tag{11}$$

The linearized Boltzmann equation (if we assume an $e^{j(\omega' t' - \bar{k}' \cdot \bar{r}')}$ dependence for f_1) is

$$j(\omega' - \bar{k}' \cdot \bar{v}')\, f_1 + \frac{q}{m}(\vec{v}' \times B_0 \bar{i}_z) \cdot \nabla_{v'} f_1 = -\frac{q}{m}\bar{E}_1' \cdot \nabla_{v'} f_0. \tag{12}$$

The dispersion relation[1] is found to be

$$0 = 1 + \frac{\omega_p^2}{k'^2}\int_0^\infty v_\perp' dv_\perp' \int_0^\infty dv_z' \sum_{m=-\infty}^{m=+\infty} \frac{J_m^2(p)}{(\omega' - k_{||}' v_z' - m\omega_c)}\left(\frac{m\omega_c}{v_\perp'}\frac{\partial}{\partial v_\perp'} + k_{||}'\frac{\partial}{\partial v_z'}\right)\frac{2\pi}{n_0} f_0(v'). \tag{13}$$

Here, if e is the magnitude of the electronic charge and n_0 the number density of electrons, ω_p is the plasma frequency $\left(\omega_p^2 = \frac{e^2 n_0}{\epsilon_0 m}\right)$, and ω_c is the cyclotron frequency $\left(\omega_c = \frac{eB_0}{m}\right)$. J_m is a Bessel function of the first kind, order m; $v_\perp' = \sqrt{v_x'^2 + v_y'^2}$; $p = \frac{k_\perp' v_\perp'}{\omega_c}$. The wave number $k_{||}'$ is the component of $\bar{k}'$ along $B_0 \bar{i}_z$, while $k_\perp' = \sqrt{k_x'^2 + k_y'^2}$.

In order to find the dispersion relation in the laboratory system, one uses the Galilean transformations for frequency and wave number:

$$\omega = \omega' + k_x' v_{0x} \tag{14}$$

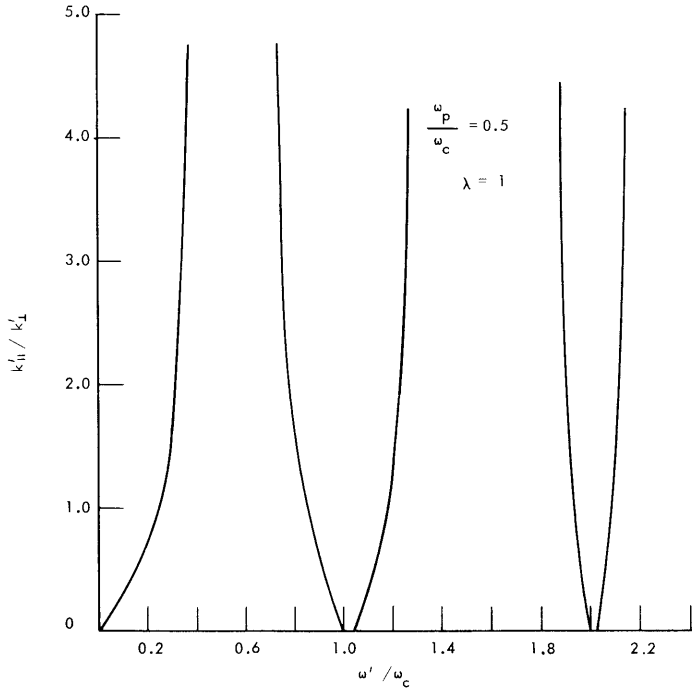

Fig. XI-8. Dispersion relation showing stable solutions.

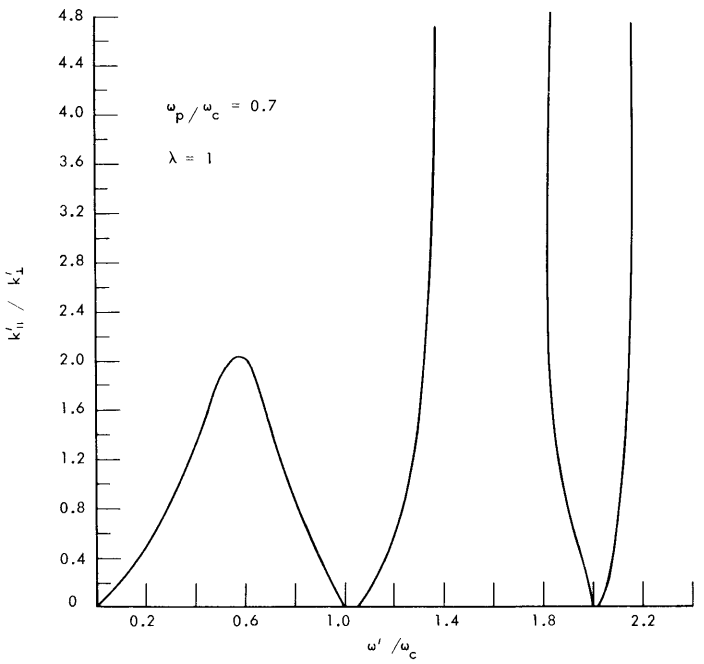

Fig. XI-9. Dispersion relation showing instability at $\omega' \approx 0.6\ \omega_c$.

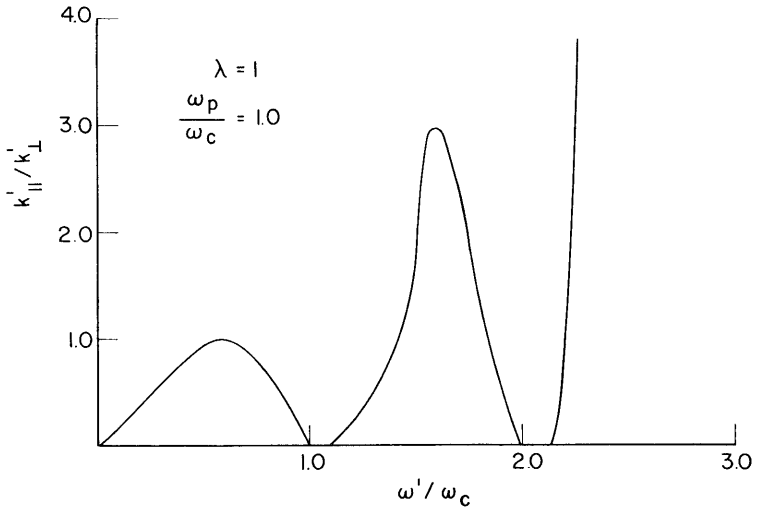

Fig. XI-10. Dispersion relation showing instabilities at $\omega' \approx 0.6\ \omega_c$ and $\omega' \approx 1.6\ \omega_c$.

$$\bar{k} = \bar{k}'. \tag{15}$$

If the unperturbed distribution function for the beam is taken as in Eqs. 1 and 10, with $g(v'_z) = \delta(v'_z)$, the dispersion relation becomes

$$\frac{k'^2_{\parallel}}{k'^2_{\perp}} = -\frac{1 - \frac{\omega_p^2}{\omega_c^2} e^{-\lambda} \sum_{n=-\infty}^{n=+\infty} I_n(\lambda) \frac{n/\lambda}{\left(\frac{\omega'}{\omega_c} - n\right)}}{1 - \frac{\omega_p^2}{\omega_c^2} e^{-\lambda} \sum_{n=-\infty}^{n=+\infty} I_n(\lambda) \frac{1}{\left(\frac{\omega'}{\omega_c} - n\right)^2}}, \tag{16}$$

where $I_n(x)$ is a modified Bessel function of n^{th} order and the quantity $\lambda = \frac{k'^2_{\perp}}{\omega_c^2}\left(\frac{k_B T}{m}\right)$.

In Figs. XI-8, XI-9, and XI-10 we show three plots of $\frac{k'_{\parallel}}{k'_{\perp}}$ versus the normalized frequency $\frac{\omega'}{\omega_c}$ for different values of $\frac{\omega_p}{\omega_c}$ at fixed $\lambda = 1.0$. For sufficiently small values of density $\frac{\omega_p}{\omega_c} < 0.7$, all values of $\frac{k'_{\parallel}}{k'_{\perp}}$ are stable. This may be seen from Fig. XI-8, where $\frac{\omega_p}{\omega_c} = 0.5$. When $\frac{\omega_p}{\omega_c} = 0.7$ (see Fig. XI-9), waves with $\frac{k'_{\parallel}}{k'_{\perp}} > 2.1$ are unstable, and the real part of the frequency lies in the range $0 < \frac{\omega'}{\omega_c} < 1$. As $\frac{\omega_p}{\omega_c}$ increases, more instabilities appear. For example, as shown in Fig. XI-10, for $\frac{\omega_p}{\omega_c} = 1.0$, waves with $\frac{k'_{\parallel}}{k'_{\perp}} > 1.0$ are unstable, with the real part of the frequency $0 < \frac{\omega'}{\omega_c} < 2.0$.

Recent work on a different problem whose results are related to these has been reported.[2]

H. M. Schneider, A. Bers

References

1. A. Bers and S. Gruber, Negative-energy plasma waves and instabilities at cyclotron harmonics, Appl. Phys. Letters 6, 27 (January 15, 1965).

2. S. Gruber, M. W. Klein, and P. L. Auer, High Frequency Velocity Space Instabilities, Research Report SRRC-RR-76, Sperry Rand Research Center, Sudbury, Mass., January 1965.

D. INSTABILITIES IN TRANSVERSE WAVES ALONG B_0 FOR BEAM-TYPE DISTRIBUTIONS

The dispersion relation for transverse electromagnetic waves propagating along a DC magnetic field on a plasma beam has been analyzed to uncover the instabilities that may exist.

An infinite system of stationary neutralizing ions penetrated by an electron beam is assumed. The velocity space distribution function of the electrons is taken to be

$$f_0(v_\perp, v_\parallel) = \frac{1}{2\pi v_{0\perp}} \delta(v_\perp - v_{0\perp})\ \delta(v_\parallel - v_{0\parallel}),$$

where $v_\perp$ and $v_\parallel$ are the velocities perpendicular to and along the magnetic field.

A simultaneous solution of the relativistic Boltzmann equation and Maxwell's equations yields the dispersion relation

$$\frac{c^2k^2}{\omega^2} = 1 - \frac{\omega_p^2}{\omega^2}\left[\frac{\omega - kv_{0\parallel}}{(\omega - kv_{0\parallel} - \omega_b)} + \frac{v_{0\perp}^2(k^2 - \omega^2/c^2)}{2(\omega - kv_{0\parallel} - \omega_b)^2}\right],$$

where a dependence, $e^{j(\omega t - kx)}$, of the field quantities is assumed, and only right-handed polarized waves are considered.

The criteria of Bers and Briggs were employed to analyze the dispersion relation.[1] Figure XI-11a shows the roots of the dispersion relation as a function of real k in the complex ω-plane. The plots were obtained on a cathode-ray tube by means of a system known as the "Kludge" associated with project MAC.[2] As k goes from $-\infty$ to $+\infty$, the locus in the ω-plane is traced from left to right as indicated in Fig. XI-11a. For large k the locus levels off at a maximum negative ω_i. Following Bers and Briggs, we find that instabilities exist over the range of real frequencies with negative imaginary parts. In order to determine the nature of the instability, the roots of the dispersion equation, for the real frequency range of interest, must be investigated in the complex k-plane.

Figure XI-11b shows the locus of roots in the k-plane as ω is varied from ω_L to ω_R. When two roots from opposite sides of the real k-axis meet, the dispersion equation has a saddle point, and an absolute instability is uncovered. When a root crosses the real axis and stops, a convective instability is indicated.

The nature of the instabilities as the parameters ω_p, $v_{0\perp}$, and $v_{0\parallel}$ are varied has been studied. For nonrelativistic velocities, the absolute instabilities, when they are present, occur at the points indicated by (A) and (B) in Fig. XI-11a. As the plasma frequency is increased the long-wavelength instability moves into the high-frequency region of the short-wavelength instability, as in Fig. XI-12a. For relativistic velocities perpendicular to the magnetic field, the two instabilities merge to form the loops shown in Fig. XI-13a.

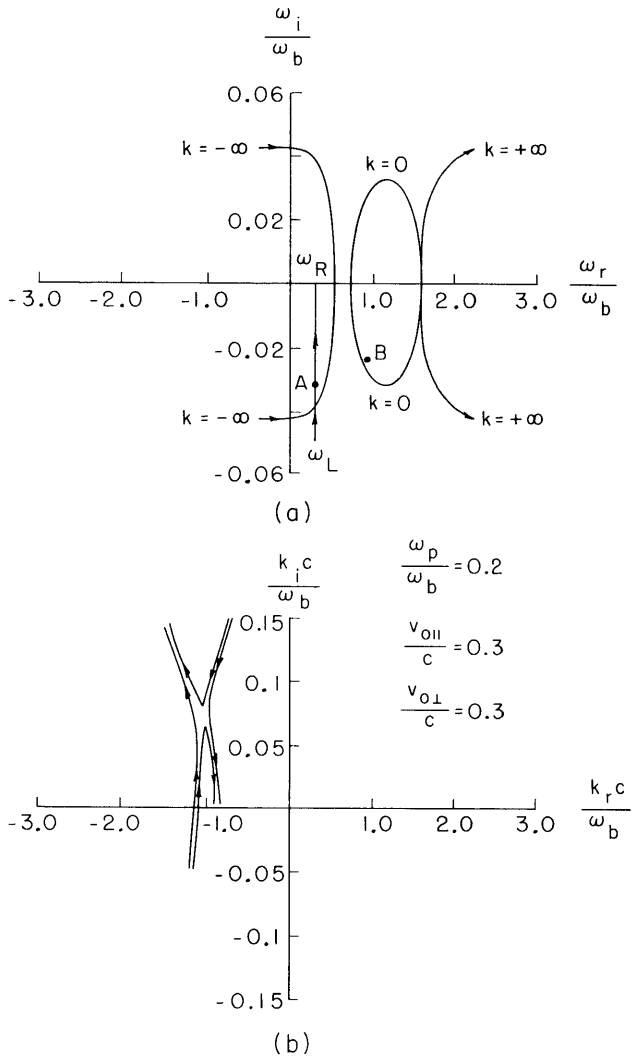

Fig. XI-11. (a) Real k-axis contours in the complex ω-plane.
(b) Complex k-plane showing the absolute instability at A.

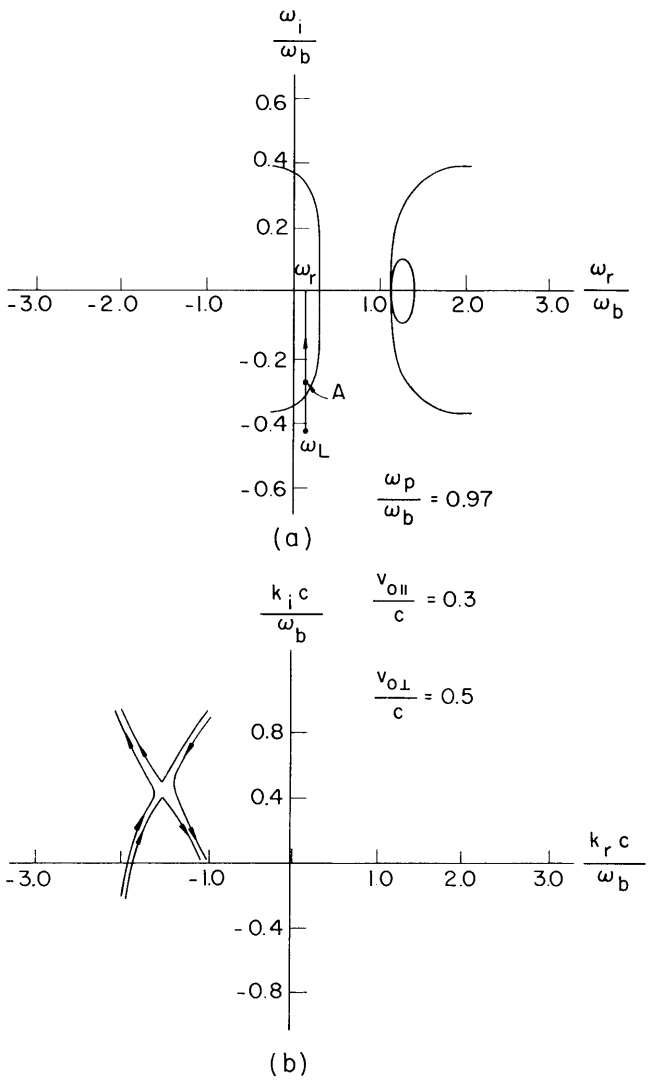

Fig. XI-12. (a) Real k-axis contours in the complex ω-plane.
(b) Complex k-plane showing the absolute instability at A.

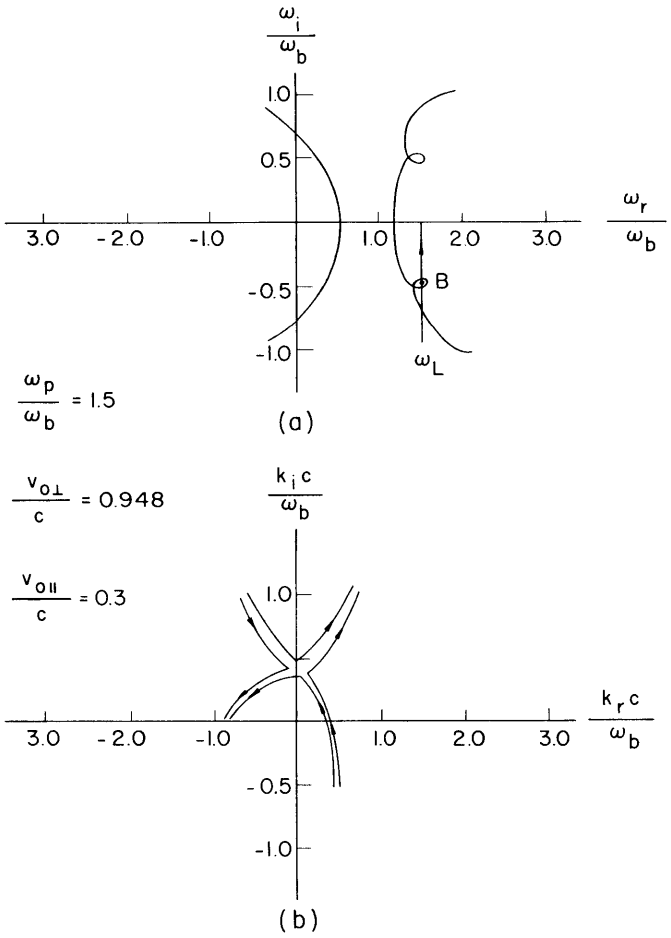

Fig. XI-13. (a) Real k-axis contours in complex ω-plane (ultra-relativistic beam).
(b) Complex k-plane showing the absolute instability at B (ultra-relativistic beam).

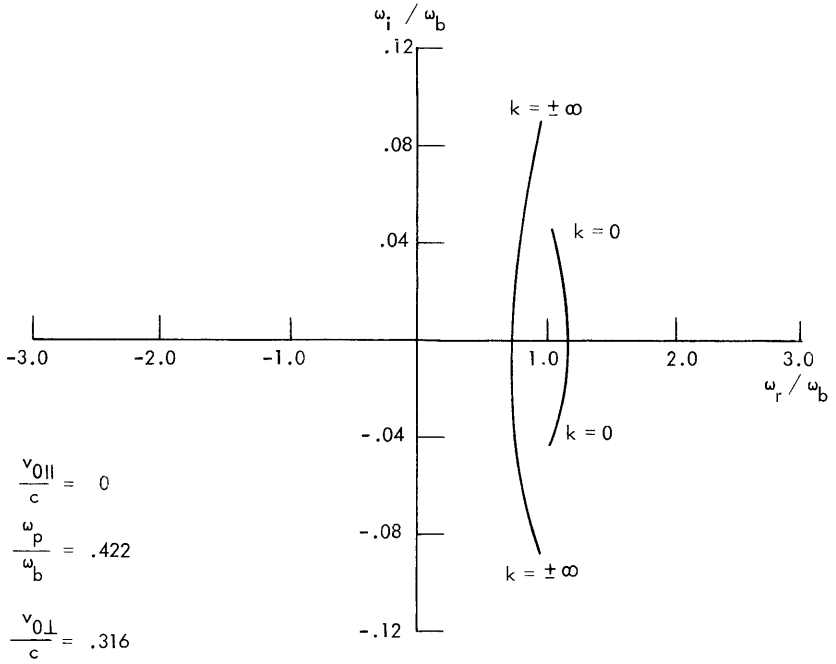

Fig. XI-14. Real k-axis contours in the complex ω-plane for $v_{0\parallel} = 0$.

For $v_{0\parallel} = 0$, the dispersion relation becomes second-order in ω and the ω-plane plots appear as in Fig. XI-14. For small ω_p the zero and infinite wave number absolute instabilities have the same value of ω_i, and the magnitude increases with ω_p. At $\frac{\omega_p}{\omega_0} \sim \frac{v_{0\perp}}{c}$ the zero wave number instabilities disappear while the large wave number solutions

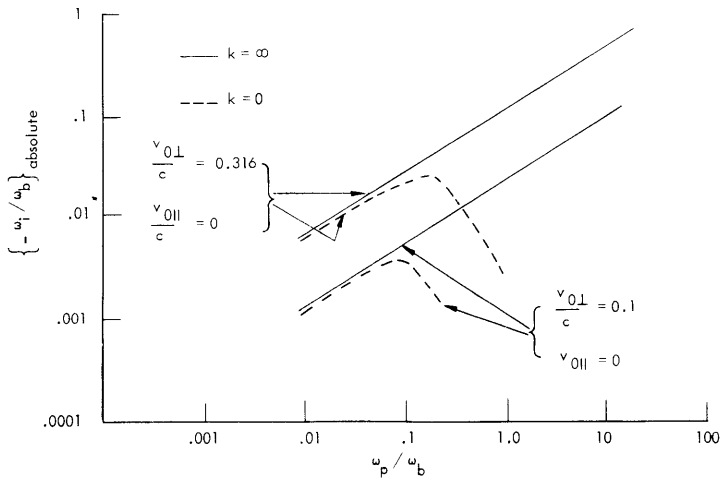

Fig. XI-15. Smooth rate of the absolute instability for $v_{0\parallel} = 0$ as a function of ω_p/ω_b, with $v_{0\perp}/c$ as a parameter.

continue to increase with ω_p. This characteristic is demonstrated in Fig. XI-15. As is also apparent from Fig. XI-15, ω_i increases with $v_{0\perp}$.

The effect of finite temperature on the instabilities discussed here is now under study.

A. Bers, J. K. Hoag, E. A. Robertson

References

1. A. Bers and R. J. Briggs, Criteria for determining absolute instabilities and distinguishing between amplifying and evanescent waves, Quarterly Progress Report No. 71, Research Laboratory of Electronics, M. I. T., October 15, 1963, pp. 122-131.

2. J. Mills and A. Bers, Computer analysis and display of wave instabilities, Quarterly Progress Report No. 73, Research Laboratory of Electronics, M. I. T., April 15, 1964, pp. 85-86.

E. HOT PLASMA WAVEGUIDES AND RESONATORS

1. Model Description

Interactions between electromagnetic fields and plasma in metallic waveguides and cavities are considered in this report. The treatement refers to a hot, collisionless, inhomogeneous electron plasma in a static magnetic field, described by the linearized first two moments of the Vlasov equation and Maxwell's equations. A scalar pressure is assumed and heat flow is neglected.

2. Dielectric-Tensor Operator

The dielectric-tensor operator K_{op} is defined[1] by

$$\overline{\overline{K}}_{op} \cdot \overline{E} = \overline{E} + \frac{\overline{J}}{j\omega\epsilon_0}. \tag{1}$$

For our model of plasma, the following expression is obtained for the dielectric-tensor operator:

$$\overline{\overline{K}}_{op} = \left(\overline{\overline{I}} - \frac{\omega_p^2}{\omega^2}\overline{\overline{A}}\right) + \frac{v_T^2}{\omega^2} n_0 \overline{\overline{A}} \cdot \nabla\left(\frac{1}{n_0}\nabla\right), \tag{2}$$

where

$$\omega_p^2 = \frac{n_0 e^2}{m\epsilon_0} \qquad \text{(electron plasma frequency)} \tag{3}$$

$$v_T^2 = \frac{k_B T}{m} \qquad \text{(electron thermal velocity)} \tag{4}$$

$$\overline{\overline{A}} = \begin{bmatrix} \frac{1}{1-\Omega_b^2} & \frac{j\Omega_b}{1-\Omega_b^2} & 0 \\ \frac{-j\Omega_b}{1-\Omega_b^2} & \frac{1}{1-\Omega_b^2} & 0 \\ 0 & 0 & 1 \end{bmatrix} \tag{5}$$

Here, $\Omega_b = eB_0/m\omega$, and the static magnetic field B_0 is directed along the z-axis.

3. Energy Conservation Principle

For the assumed lossless plasma, there exists a relation[2] between power flow S and energy W stored in a volume τ:

$$S = -\frac{d}{dt} W, \tag{6}$$

$$S = \oint_{\sigma} [\bar{E} \times \bar{\bar{H}} + mv_T^2 n\bar{v}] \cdot \bar{i}_n da \tag{7}$$

$$W = \int_V \frac{1}{2}\left[\mu_0 H^2 + \epsilon_0 E^2 + mn_0 v^2 + \frac{mv_T^2}{n_0} n^2\right] d\tau. \tag{8}$$

Here, the surface σ encloses the volume τ. Note that in these equations n_0 may be a function of position.

4. Boundary Conditions

Applying the uniqueness theorem to our model of plasma, we find that the solution will be unique if the following boundary conditions are specified:

$\bar{i}_n \times \bar{\bar{E}} = 0$ on part of the cavity or waveguide wall (perfect electric conductor) (9)

$\bar{i}_n \times \bar{\bar{H}} = 0$ on the remainder of the cavity or waveguide wall (perfect magnetic conductor) (10)

$\bar{i}_n \cdot \bar{v} = 0$ on part of the plasma interface (11)

$n = 0$ on the remainder of the plasma interface. (12)

Equations 9-12 may be derived by a technique similar to that used by Bobroff and Haus[3] for electron beams. When the boundary conditions (9-12) are satisfied, the dielectric-tensor operator $\bar{\bar{K}}_{op}$ is a Hermitian operator for the cavity or waveguide considered.

For a cavity of volume τ,

$$\int_\tau \bar{E}^* \cdot \bar{\bar{K}}_{op} \cdot \bar{E} d\tau = \int_\tau \bar{E} \cdot \bar{\bar{K}}_{op}^* \cdot \bar{E}^* d\tau. \tag{13}$$

For a waveguide of cross section A,

$$\int_A \bar{E}^* \cdot \bar{\bar{K}}_{op} \cdot \bar{E} da = \int_A \bar{E} \cdot \bar{\bar{K}}_{op}^* \cdot \bar{E}^* da. \tag{14}$$

When the conditions (9-12) are satisfied, the field solutions will be unique, except at resonances, and for systems capable of sustaining isolated plasma waves (electrostatic waves).

5. Approximate Techniques

The introduction of waveguide and cavity boundaries increases the complexity of the field analysis problem, to the point where it will be difficult or impossible to obtain

exact solutions. It is usually convenient, therefore, to use approximate methods.

a. Perturbation Theory

We compare the hot-plasma system, characterized by the dielectric-tensor operator $\overline{\overline{K}}_{op}$, with a closely related system, characterized by the dielectric tensor $\overline{\overline{K}}$ (for the cold-plasma system) and whose field variables have the subscript 0. By manipulation of Maxwell's equations for the two systems, and by using Green's theorems and the boundary conditions, we obtain relations[4] for the characteristic quantities of the system considered:

(a) Resonant frequency of a cavity

$$\omega - \omega_0 = \frac{-\omega\epsilon_0 \int_\tau \left[\overline{E}_0^* \cdot \overline{\overline{K}}_{op} \cdot \overline{E} - \overline{E} \cdot \overline{\overline{K}}^* \cdot \overline{E}_0^*\right] d\tau}{\int_\tau \left[\mu_0 \overline{H}_0^* \cdot \overline{H} + \epsilon_0 \overline{E} \cdot \overline{\overline{K}}^* \cdot \overline{E}_0^*\right] d\tau}; \tag{15}$$

(b) Cutoff frequency of a waveguide

$$\omega - \omega_0 = \frac{-\omega\epsilon_0 \int_A \left[\overline{E}_0^* \cdot \overline{\overline{K}}_{op} \cdot \overline{E} - \overline{E} \cdot \overline{\overline{K}}^* \cdot \overline{E}_0^*\right] da}{\int_A \left[\mu_0 \overline{H}_0^* \cdot \overline{H} + \epsilon_0 \overline{E} \cdot \overline{K}^* \overline{E}_0^*\right] da}; \tag{16}$$

(c) Propagation constant of a waveguide ($e^{-\gamma z}$)

$$\gamma + \gamma_0^* = \frac{j\omega\epsilon_0 \int_A \left[\overline{E}_0^* \cdot \overline{\overline{K}}_{op} \cdot \overline{E} - \overline{E} \cdot \overline{\overline{K}}^* \cdot \overline{E}_0^*\right] da}{\int_A \overline{i}_z \cdot \left[\overline{E}_0^* \times \overline{H} + \overline{E} \times \overline{H}_0^*\right] da} \tag{17}$$

Relations 15-17 are exact relations. Since the fields E and H are unknown, some approximations can be made if the perturbation is small. It is usually assumed (unless some more accurate approximation is available) that $\overline{E} \approx \overline{E}_0$, $\overline{H} \approx \overline{H}_0$. With this approximation, the denominator of (17) becomes $4P_z^{em}$, that is, four times the time-averaged power carried in the z-direction by the unperturbed wave.

b. Variational Principles

Since the dielectric-tensor operator $\overline{\overline{K}}_{op}$ is Hermitian when used with the boundary conditions (9)-(12), it is possible to derive variational principles for the characteristic quantities of the system.

(a) Resonant frequency of a cavity

$$\omega^2 = c^2 \frac{\int_\tau |\nabla \times \bar{E}|\, d\tau}{\int_\tau \bar{E}^* \cdot \bar{\bar{K}}_{op} \cdot \bar{E} d\tau}; \tag{18}$$

(b) Cutoff frequency of a waveguide

$$\omega^2 = c^2 \frac{\int_A |\nabla_T \times \bar{E}|\, da}{\int_A \bar{E}^* \cdot \bar{\bar{K}}_{op} \cdot \bar{E} da}; \tag{19}$$

(c) Propagation constant of a waveguide

$$\gamma = j\beta = \frac{\int_A \left[\bar{H}^* \cdot \nabla_T \times \bar{E} - \bar{E}^* \cdot \nabla_T \times \bar{H} + j\omega\mu_0 |\bar{H}|^2 + j\omega\epsilon_0 \bar{E}^* \cdot \bar{\bar{K}}_{op} \cdot \bar{E} \right] da}{2\,\mathrm{Re} \int_A [\bar{E} \times \bar{H}^*] \cdot \bar{i}_z da}. \tag{20}$$

This variational principle in Eq. 20 is valid only when $\gamma = j\beta$, and hence only in particular frequency regions.[5] The trial fields for the three variational principles must be continuous and differentiable, and must satisfy the boundary conditions.

Further details and applications may be found in Gardiol's thesis.[6]

F. Gardiol, A. Bers

References

1. P. E. Serafim and A. Bers, Interaction between an electron beam and plasmas, Quarterly Progress Report No. 70, Research Laboratory of Electronics, M. I. T., July 15, 1963, pp. 121-128.

2. W. P. Allis, S. J. Buchsbaum, and A. Bers, Waves in Anisotropic Plasmas (The M. I. T. Press, Cambridge, Mass., 1963).

3. D. L. Bobroff and H. A. Hauss, Uniqueness and Orthogonality of Small Signal Solutions in Electron Beams, Technical Report No. 31, Research Division, Raytheon Company, Waltham, Mass., 1958.

4. B. Lax and K. Button, Microwave Ferrites and Ferri-magnetics (McGraw-Hill Publishing Company, New York, 1962).

5. W. P. Allis, S. J. Buchsbaum, and A. Bers, op. cit., p. 176.

6. F. Gardiol, Approximate Techniques for Hot Plasma Waveguides and Resonators, S. M. Thesis, Department of Electrical Engineering, M. I. T., January 1965.

F. EMISSION PROCESSES BY AN OSCILLATOR MOVING AT SUPER-WAVE VELOCITY

When an oscillator is moving relative to a medium through which a certain kind of wave is propagating, it emits or absorbs a quantum, which is associated with the wave

field. The energy of an emitted quantum depends upon the relative velocity, as well as the characteristic frequency of an oscillator according to the Doppler effect. But if the relative velocity exceeds the phase velocity of the wave, qualitatively new phenomena appear. One of them has already been pointed out and discussed by Ginzburg, Eidman, and Zheleznyakov[1,2] as the "anomalous Doppler effect." The anomalous Doppler effect can be explained either classically or quantum mechanically. In this report other new phenomena will be discussed which have no classical analogues in this velocity region.

In the interaction between a single oscillator and a wave field if the diagonal elements of the interaction Hamiltonian between an oscillator and a wave field are zero with respect to the unperturbed eigenstates, the total momentum and energy are conserved in the emission or absorption processes.

$$\sum_{\lambda} n_{\lambda} h k_{\lambda} + \overline{P} = \text{const} \tag{1}$$

$$\sum_{\lambda} n_{\lambda} h \omega_{\lambda} + \frac{\overline{P}^2}{2M} + W = \text{const}, \tag{2}$$

where n_{λ}, $\overline{k}_{\lambda}$, ω_{λ} are the quantum number, wave vector, and frequency, respectively, of the wave mode specified by λ; $\overline{P}$, M, W are the momentum, the mass, and the internal energy, respectively, of the oscillator. Assuming that only one mode of the wave field is involved in the present process, and the wave vector is parallel to P, we have

$$W = \text{const} - \frac{1}{2M}(P-MU)^2, \tag{3}$$

where $U = \omega_{\lambda}/k_{\lambda}$ is the phase velocity. This is shown in Fig. XI-16.

This is a locus on which the momentum and the internal energy of the oscillator are confined during the interaction.

Let us consider only the emission processes, since the absorption occurs in the direction opposite to the emission on this locus. The internal energy of the oscillator is supposed to be changed by ΔW.

1. When the oscillator state is at 1 initially, it goes down the slope to 2 after emission of a quantum with a momentum hk_{λ}, as required by Eq. 1. In this process W always decreases. This sort of process is called the "normal Doppler effect."

2. When the oscillator is moving slight faster than the phase velocity and located at 3, it can make a transition to 4 without losing its internal energy. This is a Cherenkov type of emission process.

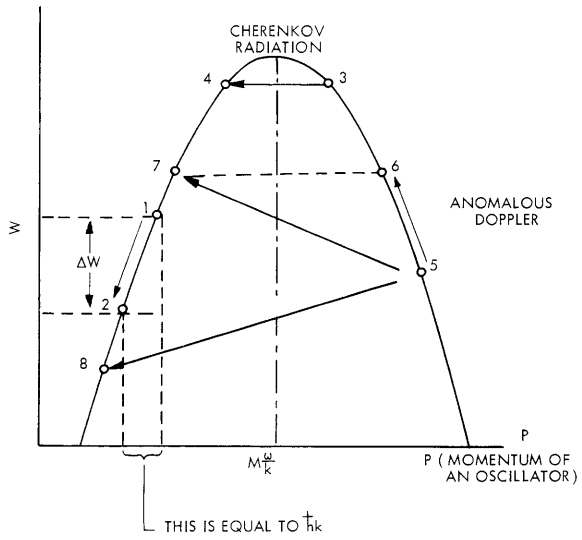

Fig. XI-16. Diagram of transitions.

3. When the oscillator velocity largely exceeds the phase velocity of the wave which is located at 5 it can make three different transitions. A transition 5 → 6 is called the anomalous Doppler effect, in which the final velocity of the oscillator is always larger than U and the internal energy of the oscillator is always increased. On the other hand, in a process 5 → 7, the oscillator increases the internal energy and at the same time is decelerated to a velocity smaller than U. The other possibility is a process 5 → 8, in which the oscillator loses its internal energy as well as its kinetic energy. In the last two processes the internal state of the oscillator goes through an energy tunnel to a final state, and we have no classical analogues for them. A possible example will be found in the interaction of phonons with gyrating conduction electrons in a DC magnetic field. These processes occur spontaneously or through stimulation by the wave field.

T. Musha

References

1. V. L. Ginzburg and V. Ya. Eidman, Soviet Phys. – USP 2, 874 (1960).

2. V. L. Ginzburg, V. V. Zhalenznyakov, and V. Ya. Eidman, Phil. Mag. 7, 451 (1962).

G. ELECTRON CYCLOTRON RESONANCE DISCHARGE*

1. NEW MICROWAVE TECHNIQUE FOR MEASURING ELECTRON DENSITY

Since the last report[1] a new perturbation method of measuring the electron density of a plasma in a resonant cavity has been developed. The method is a variation of the method developed by Rose and Brown,[2] wherein the plasma shifts the resonant frequency of a cavity mode by changing the complex dielectric constant of the medium filling the cavity. The new method uses perturbations of many of the higher order cavity modes to measure the density of the plasma. The theory of the measurement is particularly simple.

Consider a resonant cavity partially filled with plasma which is excited at the resonant frequency of the n^{th} higher order mode. Assume that there is no steady magnetic field, or, if one is present, that the ratio of the electron cyclotron frequency to the applied frequency is negligible compared with one. Then, according to Rose and Brown, the determining ratio $\Delta f/f$ of the n^{th} mode as a result of the presence of the plasma is given by

$$\frac{\Delta f}{f} = \frac{\int_{V_p} \omega_p^2(\bar{r}) |\hat{e}_n(\bar{r})|^2 \, d^3\bar{r}}{2\omega^2 V_c}.$$

where $\omega_p(\bar{r})$ is the electron plasma frequency as a function of position, ω is the unperturbed resonant frequency of the n^{th} mode, V_c and V_p are the cavity and plasma volumes, and $\hat{e}_n(\bar{r})$ is the eigen electric-field vector of the n^{th} mode. Here the normalization

$$\int_{V_c} |\hat{e}_n(r)|^2 \, d^3\bar{r} = V_c$$

is assumed.

Now if the volume of the plasma V_p is large compared with a cubic half-wavelength at the resonant frequency of the n^{th} mode, the integral can be evaluated as

$$\int_{V_p} \omega_p^2(\bar{r}) |\hat{e}_n(r)|^2 \, d^3\bar{r} = \omega_p^2 V_p,$$

where ω_p^2 is the average density of the plasma over the volume V_p. If Δf is considerably larger than the frequency separation between modes near the frequency f, the

*This work was supported in part by the United States Atomic Energy Commission under Contract AT(30-1)-3221.

plasma will cause many modes to sweep past a given frequency f. Thus if δf is the average mode separation, the total frequency shift Δf of the n^{th} mode is given by

$$\Delta f \cong m\delta f,$$

where m is the number of modes that sweep past a given frequency f_o. The relation will be most accurate if m is much greater than one. Thus we are led to the relation

$$(\omega_p/\omega)^2 = -\frac{2m\delta f}{f}\frac{V_c}{V_p}.$$

Experiment

Two X-band waveguides were attached to the resonant box of the ECRD and microwave energy at approximately 9.5 Gc was coupled through the box and observed with a

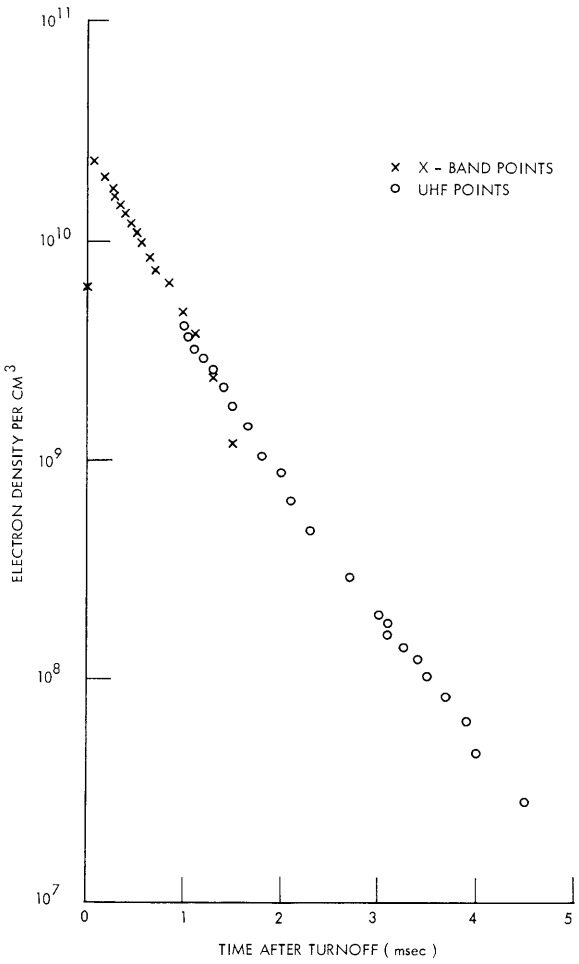

Fig. XI-17. Plasma electron density between microwave pulses.

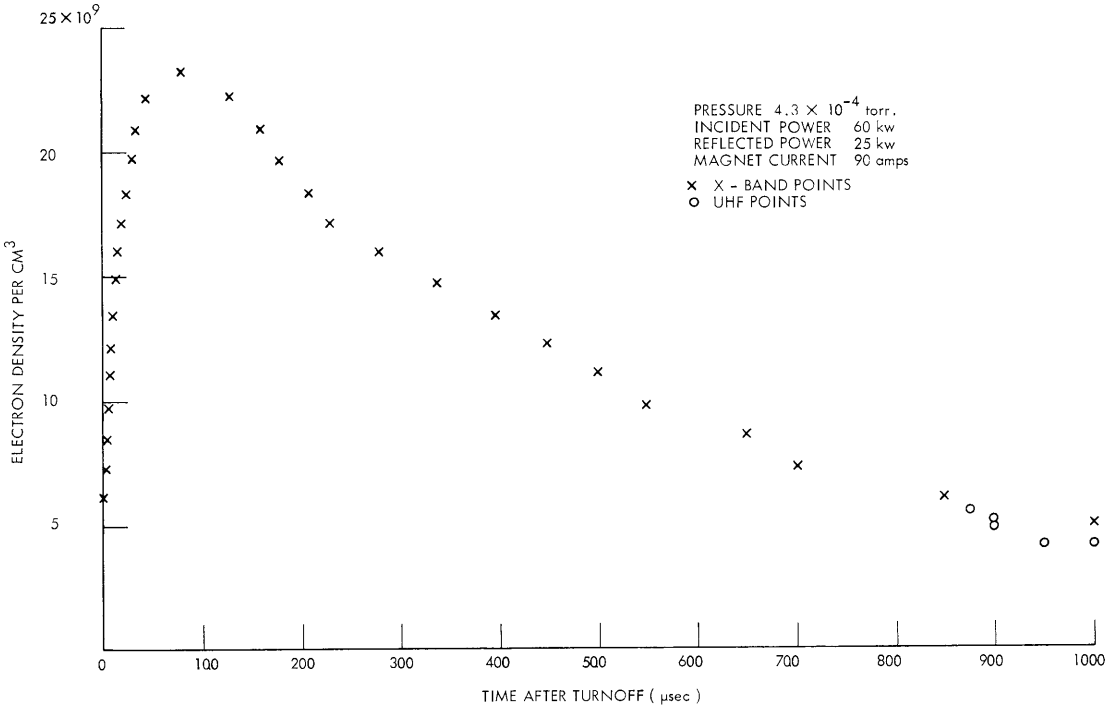

Fig. XI-18. Plasma electron density after turnoff measured with the X-band and UHF probing mode techniques. The plasma is assumed to lie in a cylinder 10 inches in diameter on the cavity axis.

crystal detector and an oscilloscope. As the frequency of the X-band energy was varied slightly, peaks in energy transmission were detected when different modes of the cavity were exactly at resonance. The mode number of these modes is approximately 10,000, and their separation was measured to be 1.69 mc/mode averaged over 100 modes, with a 10-mode maximum average of 1.98 mc/mode and a minimum of 1.27 mc/mode.

The discharge was run in the burst mode[1] and the plasma tuning of the X-band modes was observed in the afterglow after the last S-band power pulse. The parameter Δf was measured as a function of time by counting the number of modes after a given time which could be detected sweeping by the frequency 9.5 Gc. By using Eq. 1, the plasma density was calculated; some typical results are presented in Figs. XI-17 and XI-18. A comparison of results of this technique and of the UHF probing mode technique[1] is made in Fig. XI-18. In obtaining these points, all parameters of the system were carefully adjusted until they were reproducible on a pulse-to-pulse basis.

T. J. Fessenden

References

1. T. J. Fessenden, Quarterly Progress Report No. 76, Research Laboratory of Electronics, M.I.T., January 15, 1965, pp. 125-128.

2. D. J. Rose and S. C. Brown, J. Appl. Phys. 23, 1028-1032 (1952).

2. INTENSITY MEASUREMENTS OF THE ARGON 4880 Å LINE*

Intensity measurements of incoherent light emitted from an argon plasma have been made. The frequencies of particular interest were those used in argon lasers, specifically the 4880 Å and 5150 Å lines. The 5150 Å line, however, was never observed in the plasma studied here, and so the following results are for the 4880 Å line of ionized argon.

The argon plasma was created by an electron cyclotron discharge with approximately 60 watts of incident RF power at 2.8 kmc. The plasma was confined by a rectangular cavity and a symmetric magnetic mirror (see Fig. XI-19). The field strength ratio of

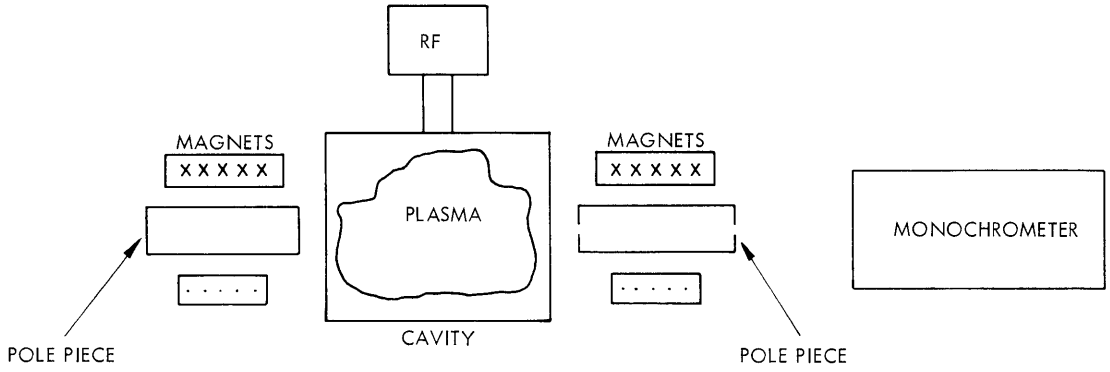

Fig. XI-19. Experimental arrangement.

the mirror was approximately 5:3. With this fixed ratio the field strength at the center of the cavity was varied from 500 gauss to 1000 gauss. The base pressure was approximately 5×10^{-6} mm Hg, and the discharge was studied at working pressures of 5×10^{-4}-5×10^{-5} mm Hg. A 3/4 inch hole was placed in one of the pole pieces and the light intensity emitted along the axial directions of the magnets was observed by a monochrometer set at 4880 Å. The output of the monochrometer was recorded for various values of the magnetic field and plasma density.

The monochrometer was then calibrated by a standard General Electric tungsten lamp. Using this calibration, we converted each plasma measurement to a value of n, which is the number of radiators per unit time per unit volume giving off a quantum of energy at 4880 Å. These results are shown in Figs. XI-20 through XI-22.

*This work was supported in part by the United States Atomic Energy Commission under Contract AT(30-1)-3221.

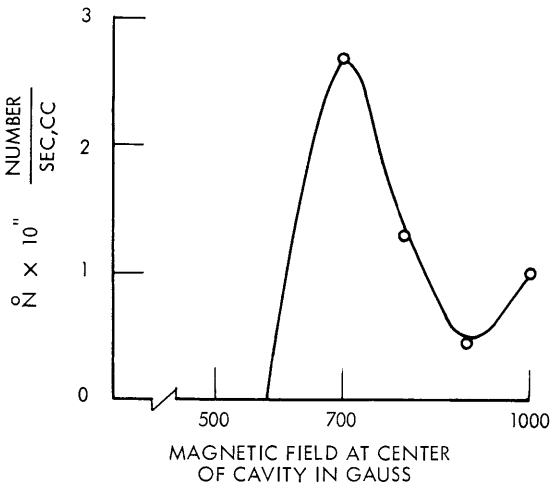

Fig. XI-20. 4880 Å line argon intensity (5×10^{-4} mm Hg).

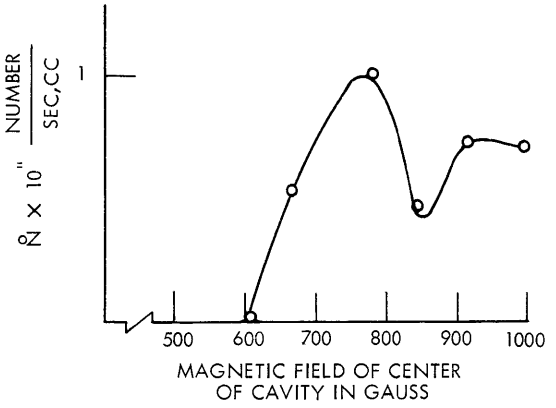

Fig. XI-21. 4880 Å line argon intensity (1×10^{-4} mm Hg).

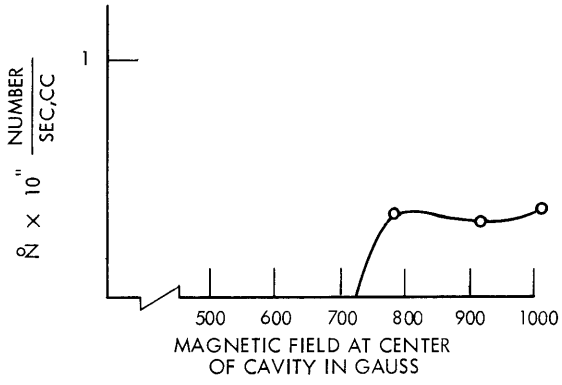

Fig. XI-22. 4880 Å line argon intensity (5×10^{-5} mm Hg).

We plan to continue this work and investigate the feasibility of pumping an argon laser with a cyclotron or beam-plasma discharge.

B. R. Kusse

H. FUSION BLANKET RESEARCH

With the completion of the doctoral thesis of L. M. Petrie, the initial phase of this work has been completed. The substantive content of five theses in this area of research, which have been submitted to the Department of Nuclear Engineering, M. I. T., in partial fulfillment of the requirements for the degrees indicated below, will be published in the Research Laboratory of Electronics technical report series. A list of authors and titles follows.

A. J. Impink, Neutron Economy in Fusion Reactor Blanket Assemblies
Ph. D. Thesis, January 1963, to appear as Technical Report 434.

W. G. Homeyer, Thermal and Chemical Aspects of the Thermonuclear Blanket Problem
Sc. D. Thesis, December 1962, to appear as Technical Report 435.

L. M. Lontai, A Study of a Thermonuclear Reactor Blanket with Fissile Nuclides
S. M. Thesis, May 1963, to appear as Technical Report 436.

P. S. Spangler, Fusion Reactor Blanket Experiment
Sc. D. Thesis, February 1965, to appear as Technical Report 437.

L. M. Petrie, Gamma Ray Spectra in Fusion Blanket Mock-ups
Sc. D. Thesis, March 1965, to appear as Technical Report 438.

D. J. Rose

I. NONADIABATIC DIFFUSION IN TOROIDAL GEOMETRY

An apparatus is being built to produce a circulating electron current in toroidal geometry by nonadiabatic injection of a cw electron beam. Although partly motivated by the problem of cw injection into closed geometry, our major objective is a study of the effect of small nonadiabatic perturbations on particle diffusion in space and velocity. A circulating beam is an ideal medium for these studies because of the simple relations between diffusion coefficients and beam lifetime.

1. Nonadiabatic Scattering

The motion of charged particles is said to be adiabatic when the magnetic fields change slowly enough along the particle trajectory. In this case, both μ, the magnetic moment, and J, the longitudinal invariant, may be treated as constants of the motion. The particle trajectory is then well described by the guiding-center approximation which predicts, except for electrical and gravitational drifts, particle motion along surfaces of fixed μ and J. If the adiabatic conditions are violated, the adiabatic invariants suffer a random fluctuation with a resultant diffusion. The nonadiabatic motion depends, as the adiabatic motion does not, on the detailed relation between the particle's phase in its motion around the guiding center and the shape and extent of the field perturbations.

Several theoretical analyses of this process have appeared[1,2] but no definitive experimental work has been done.

2. Experiment

The device will be a race track with 6 m circumferential length, and 10-cm minor diameter (see Fig. XI-23). The electron injection energy will be 4 kev to yield a 2-cm

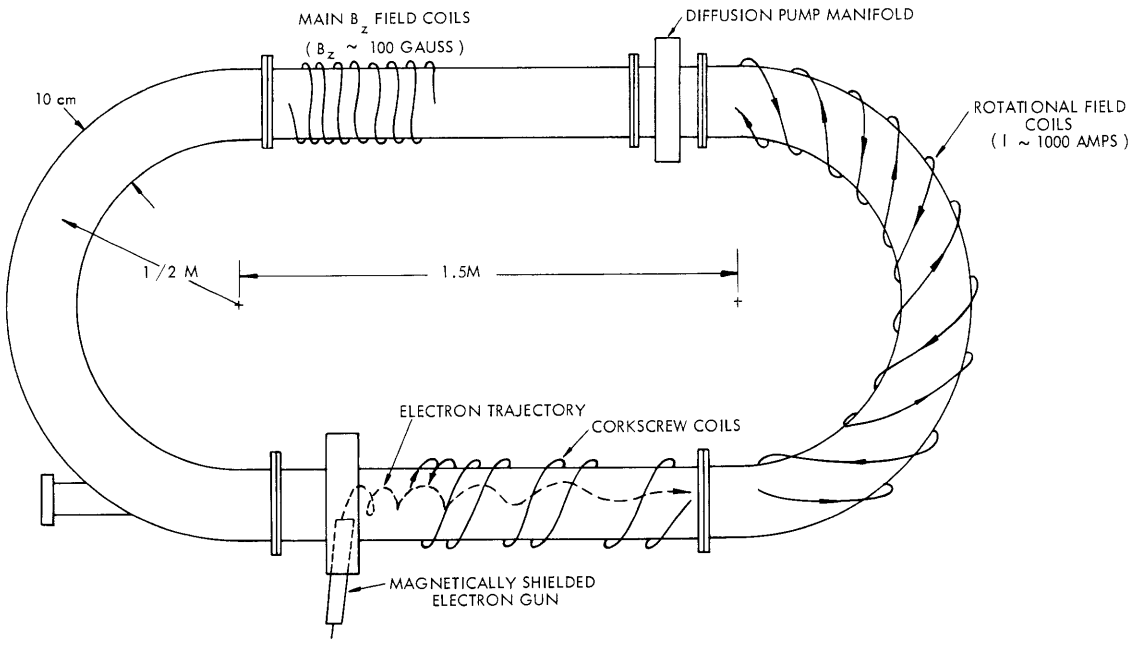

Fig. XI-23. Toroidal magnetic trap.

Larmor radius with the planned main field of 100 gauss. The electrons will be injected essentially perpendicularly to the field with only enough $v_{\parallel}$ to miss the gun snout after one orbit. They will then enter an accelerating corkscrew[3,4] which, by cumulative nonadiabatic perturbations, will increase $v_{\parallel}$ at the expense of $v_{\perp}$, so that in one pass the motion will be almost entirely along B.

The injected electrons would undergo severe curvature drifts in the U bends of the torus if no corrective action were taken. The drift distance for a particle of Larmor radius r_b is πr_b for complete traversal of the bend. In our system, because of the nature of the corkscrew injection scheme, the electron Larmor orbit is comparable to the minor diameter of the torus, and, therefore, this amount of uncorrected drift would be intolerable. Hence, we shall make use of helical windings to impart a rotational transform to the magnetic field lines. These differ from the windings found on Stellarator-type devices in that we cannot rely on drift cancellations over many transits

of the entire system but must cancel drifts within a single U bend. To study these complicated particle trajectories, we have developed a computer program to integrate the equations of motion and to determine the magnetic field surfaces. Figure XI-24 shows the motion of a particle in a U bend with a 2π rotational transform. The important

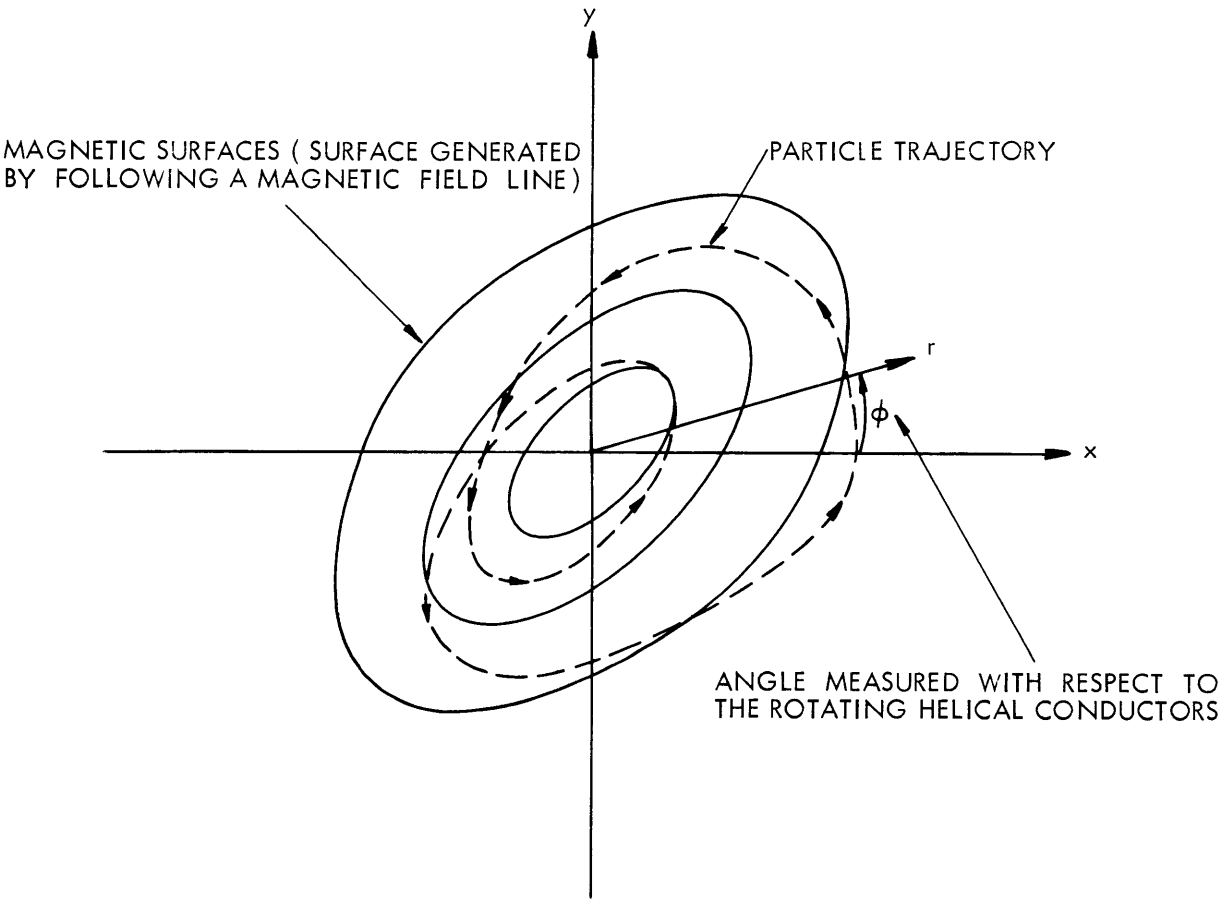

Fig. XI-24. Two dimensional projection of a trajectory and magnetic surfaces with a rotational transform of 2π.

quantity is the radial component of the vector connecting the particle position at the beginning and end of its transit through the U bend. Figure XI-25 shows the effect of many transits through a U bend, illustrating the order of magnitude of the remaining spatial diffusion effects for one particular choice of helical transform strength. Our aim is to make particle losses caused by imperfections in the drift cancelling scheme small compared with those resulting from nonadiabatic losses from the corkscrew or other intentionally introduced perturbations that are to be studied.

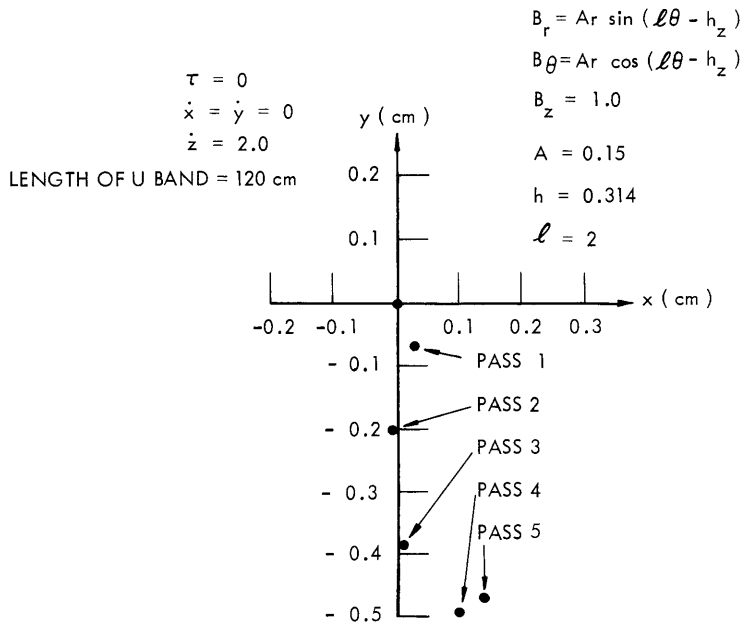

Fig. XI-25. Cumulative plot of residual drifts after multiple passes through a U bend with rotational transform of 2π at r = .5 cm.

Principal diagnostic methods will involve Rogowsky coils for detection of the modulated circulating beam and flourescent screens for visual location of beam position.

R. W. Moir, L. M. Lidsky

References

1. R. C. Wingerson, T. H. Dupree, and D. J. Rose, Phys. Fluids 7, 1475 (1964).

2. A. F. Laing and B. M. Robson, J. Nucl. Energy, Part C, 3, 146(1961).

3. L. M. Lidsky, Phys. Fluids 7, 1484 (1964).

4. C. Kapetanakos, S.M. Thesis, Department of Nuclear Engineering, M.I.T., August 1964.

J. PLASMA TURBULENCE STUDIES

The construction of the Hollow-Cathode Discharge III device described in Quarterly Progress Report No. 76 (pages 130-133) has been completed. The magnet coils have been tested successfully and maximum field in excess of 4 Kgauss can be obtained over the region of interest. The profile of the axial field on the centerline of the system and at the wall of the vacuum chamber is shown in Fig. XI-26.

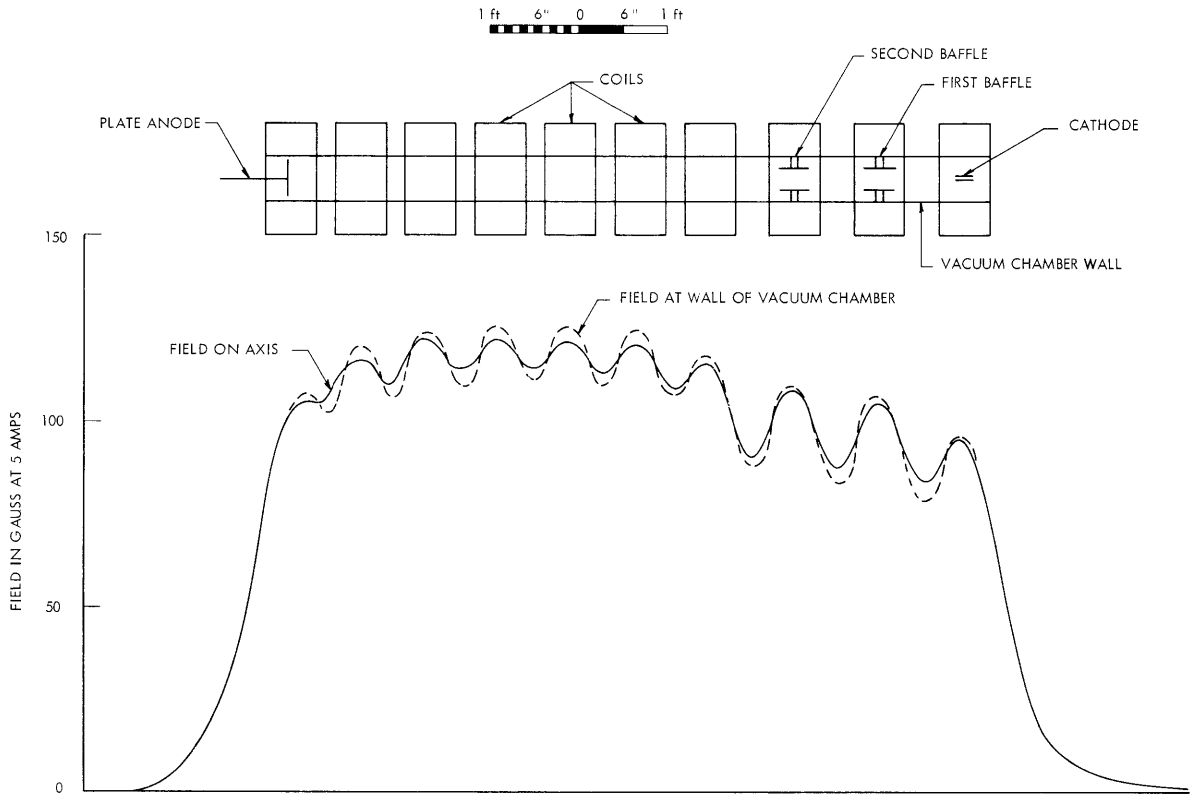

Fig. XI-26. Profile of axial field of HCD III system.

Shims are now being installed to minimize the variations in the axial field, after which the device will be operational. The first phase of experiment will be the determination of operating parameters of the plasma; the next phase will be the turbulence studies.

J. C. Woo

K. STUFFED-CUSP PLASMA FACILITY

Construction has begun on a "stuffed-cusp" magnetic trap. This is a "minimum B" system consisting of a simple spindle cusp with an axial conductor. The axial current creates a system with a nonzero minimum of induction which should enhance the single-particle (adiabatic) containment properties of the cusp.

We propose to generate a plasma inside the device by injecting an electron beam through the line cusp and making use of the beam-plasma interaction. In this manner, we hope to generate a hot electron plasma with densities of the order of $10^{12}/cm^3$. If this scheme fails to work, microwave equipment is available to create a plasma by electron-cyclotron resonance heating. The resonant frequency then can be adjusted so

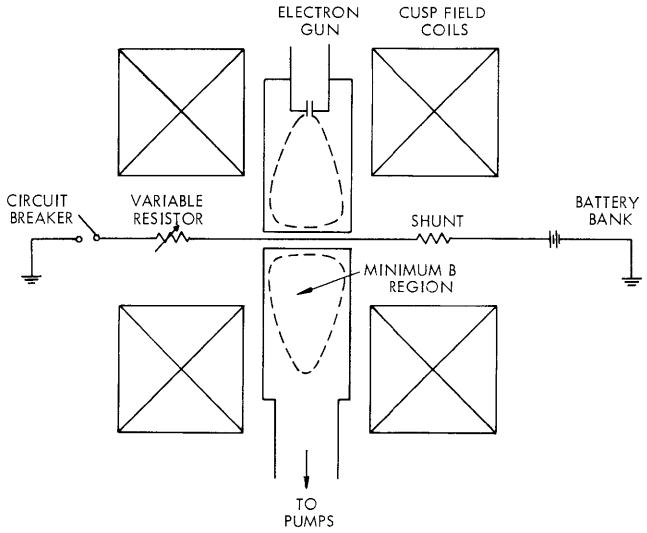

Fig. XI-27. Schematic diagram of the stuffed cusp.

that the heating region coincides with the center of the containment volume.

A schematic diagram of the facility is shown in Fig. XI-27. The cusp field will be generated by two existing tape-wound coils driven by a 60-kw generator. Axial current will be furnished by a bank of 12-v storage batteries which will give 14.7 kA through the water-cooled copper central conductor. A circuit breaker will be constructed employing a dielectric slab driven between movable electrodes. Interchangeable resistor links consisting of stainless-steel and copper tubes will be used to make fine adjustments in current.

The resulting magnetic field configuration, computed by using the MAFCO code,[1] is plotted in Fig. XI-28. The largest closed magnetic isobar is 1.16 kgauss, while the minimum induction is 0.62 kgauss; this gives a mirror ratio of 1.9.

A cylindrical stainless-steel vacuum can (24-inch diameter × 7 inches) has been constructed with 7 radial ports. A removable vacuum wall has been built around the central conductor so that the conductor may be withdrawn and the system run as a simple cusp. A 4-inch oil-diffusion pump and baffle that give a pumping speed of 300 liters/sec have been installed.

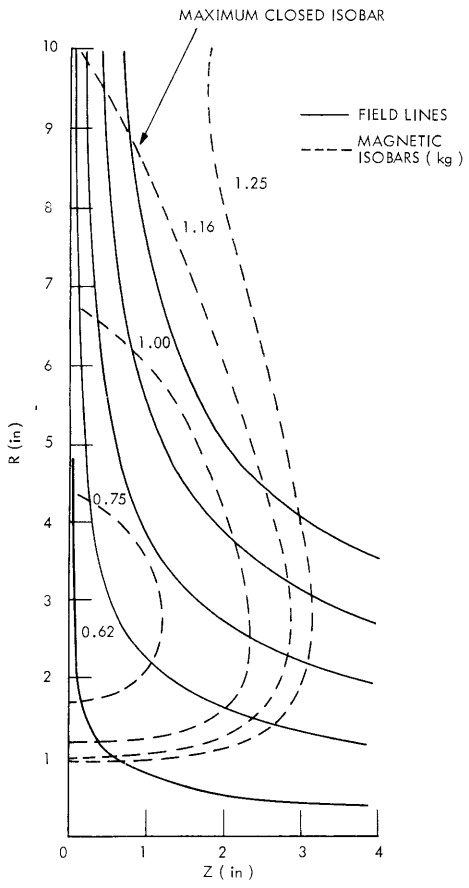

Fig. XI-28. Magnetic field plot.

Proposed diagnostic techniques for the facility are microwave interferometry; x-ray, light, and RF spectral measurements; and single-particle detection with scintillation or solid-state counters.

We propose to study the effect of a nonzero minimum of the induction on the stability and containment properties of a cusp. Also, studies of the beam-plasma interaction or of electron-cyclotron heating in this geometry may be performed.

C. E. Wagner, L. M. Lidsky

References

1. The MAFCO code was developed at Lawrence Radiation Laboratory, Livermore, California.

L. MOTION IN NONADIABATIC FIELDS*

Let us consider a charged particle moving in a magnetic field which has a characteristic length of the order of the particle's Larmor radius. The particle's magnetic moment will no longer be conserved; as a result, an external beam can be trapped between magnetic mirrors. The phenomenon is widely recognized and has formed the basis of many publications.[1-4] In this report we attempt to obtain further insight into the interaction by studying the equation of motion,

$$\frac{d\vec{v}}{dt} = \vec{v} \times \vec{\omega}; \qquad \vec{\omega} = \frac{e\vec{B}}{m} \tag{1}$$

in curvilinear coordinates running along the field lines. The coordinate system is obtained by defining the unit vectors $\hat{t}$, $\hat{n}$, and $\hat{b}$, where $\hat{t}$ is along the field direction, n is in the direction of the principal normal, that is, in the direction of the instantaneous radius of curvature, and $\hat{b}$ is in the direction of the bi-normal, that is, the direction in which the field lines twist. These vectors are related by the Frenet-Seret formulas

$$\begin{aligned} \frac{d\hat{t}}{ds} &= \kappa \hat{n} \\ \frac{d\hat{n}}{ds} &= -(\kappa \hat{t} + \tau \hat{b}) \\ \frac{d\hat{b}}{ds} &= \tau \hat{n} \end{aligned} \tag{2}$$

where κ is the inverse radius of curvature, τ is a measure of the torsion, and s is a measure of arc length along the field lines. As a result of employing these relations and the definition

$$ds = v_t dt \tag{3}$$

the equation of motion becomes

$$\frac{dv_t}{ds} = \kappa v_n \tag{4a}$$

$$\frac{dv_n}{ds} = -\kappa v_t + \left(\frac{\omega}{v_t} - \tau\right) v_b \tag{4b}$$

$$\frac{dv_b}{ds} = -\left(\frac{\omega}{v_t} - \tau\right) v_n. \tag{4c}$$

---

*This work was supported in part by the United States Atomic Energy Commission (Contract AT(30-1)-3285).

These equations can be simplified by defining $v_t = v_n + jv_b$ and combining (4b) and (4c) to obtain

$$\frac{dv_+}{ds} = -\kappa v_t - j(\beta-\tau)\, v_+ \tag{5a}$$

$$\frac{dv_t}{ds} = \kappa v_n, \tag{5b}$$

where $\beta = \omega/v_t$. For a weak nonadiabatic perturbation, the change in the particle's magnetic moment per transit will be small unless some resonance occurs. The obvious approximation is to assume v_t to be constant. Then (5a) and (5b) uncouple, and we can treat κ, τ, and β as known functions that specify the magnetic field. The physical meaning of (5a) is clear if we convert from a space to a time description,

$$\frac{dv_+}{dt} + j(\omega - v_t\tau)\, v_+ = -\frac{v_t^2}{R}. \tag{6}$$

Since $\kappa = 1/R$, we see that the force that changes the magnitude of the perpendicular velocity is due to the centripetal acceleration experienced when the particle attempts to follow the perturbed field lines. The phase of the particle's rotation is specified by the imaginary term, and this is affected by both the magnitude of the field and its torsion.

A direct integration gives

$$\Delta v_+ = -\int_0^L \kappa v_t \exp -j\left\{\int_s^L (\beta-\tau)\, ds'\right\} ds, \tag{7}$$

which is the desired result, the change in the perpendicular velocity resulting from a transit through the perturbation.

The physical content of Eq. 7 is most easily visualized by comparison with the formal solution of the equation of radiative transfer:

$$\Delta I = \int_0^L \eta \exp -\left\{\int_s^L \alpha\, ds'\right\} ds, \tag{8}$$

where I is radiative flux, η is the emissivity, and α is the absorption per unit length. The total change of flux in a beam traversing an active medium is given by summing, at the end point, the contribution of the emission at each point on the path diminished by the absorption of that quantum over the remaining path length. Referring to Eq. 7, we see that the effect of the perturbation can be interpreted in an analogous manner. The change in v_+ produced by the curvature at each point on the particle's trajectory is

added at the end of the perturbation with an appropriate phase determined by the factor $(\beta-\tau)$ which is the net rotation per unit path length.

Let us now consider the particular example of the stellarator type of field which, near the axis, can be represented by

$$\omega_r = \omega_o h(kr)^{\ell-1} \sin(\ell\theta - kz)$$

$$\omega_\theta = \omega_o h(kr)^{\ell-1} \cos(\ell\theta - kz) \tag{9}$$

$$\omega_z = \omega_o (1 + h(kr)^{\ell} \cos(\ell\theta - kz)).$$

Here θ is the particle's azimuthal position, and h is a smallness parameter. We assume that (kr) is also small and approximately constant over the particle orbit. Neglecting terms in h^2 compared with h, we find

$$\kappa = h(kr)^{\ell-1} \left\{ k - (\ell-1) \frac{\partial\theta}{\partial z} \right\} \tag{10a}$$

$$\tau = \left\{ k - (\ell-1) \frac{\partial\theta}{\partial z} \right\}. \tag{10b}$$

If we consider a particle moving along a field line with only a small perpendicular velocity, we can assume that θ is a constant. Then (7) gives

$$\Delta v_+ = -h(kr)^{\ell-1} k v_t \int_0^L \exp -j\left\{ (\beta-k)\, z + \left(\frac{\beta}{k}\right) h(kr)^{\ell} \sin(\ell\theta - kz) \right\} dz. \tag{11}$$

The resonant nature of the interaction is evident from the $(\beta-k)$ term in the exponent. This measures the phase of the particle relative to the field. Because the field curvature is constant, the particle sees a force of constant magnitude and if it rotates with the field $(\beta=k)$, its phase relation to this force is preserved. Therefore a large transfer can occur between its parallel and perpendicular kinetic energy. The second term in the exponent is of higher order and represents the change in phase caused by a variation in the magnitude of the particle's cyclotron period as the main field fluctuates.

We consider now a bumpy mirror type of field given by

$$\omega_z = \omega_o (1 + h \sin kz)$$

$$\omega_r = -\frac{(kr)}{2} \omega_o h \cos kz. \tag{12}$$

Employing the same assumptions as before, we find

$$\kappa = kh\left(\frac{kr}{2}\right) \sin kz$$

$$\tau = 0 \tag{13}$$

and the interaction is described by

$$\Delta v_+ = -kh\left(\frac{kr}{2}\right) v_t \int_0^L \sin kz \exp -j\left\{\beta z - \left(\frac{\beta}{k}\right) h \cos kz\right\} dz. \tag{14}$$

We see that now the basic resonance is caused by a variation of the field curvature along the particle's trajectory. Thus we can see a basic difference in these two interactions. In the case of stellarator fields the particle experiences a constant centripetal force, and it is the twist of the field lines which determines the resonance by adding the velocity changes in phase. In the bumpy-mirror case the phase propagation is independent of the perturbation, but the curvature force fluctuates in space so that the velocity changes from different parts of the orbit will add in phase at the end point.

This manner of thinking suggests a method of attack for minimizing the velocity change for trapped particles. Although κ and τ are not independent, a consideration of their different natures suggests that their effects may be made to cancel for specific particle velocities. If this velocity is chosen near the loss cone, the possibility exists of reducing the scattering of particles past that velocity by the perturbation. The ultimate particle lifetime would then be determined by other mechanisms.

In addition to its function as a guide to an intuitive understanding of nonadiabatic interactions, Eq. 7 can also be used to explain the complicated subresonances observed in some recent trapping experiments.[5] These subresonances appear when it becomes necessary to discard the assumption that θ is a constant. This occurs when the particle acquires enough perpendicular velocity so that its Larmor orbit becomes comparable with the characteristic lengths of the field. In the experiment performed by Demirkhanov and his co-workers,[5] a constant pitch $\ell = 3$ stellarator field was used. Rewriting (11) with the full form of (10b), we obtain

$$\Delta v_+ = \int_0^L \kappa v_t \exp -j\left\{(\beta_o - k) z + (\ell - 1)\theta + \left(\frac{\beta}{k}\right) h(kr)^{\ell} \sin(\ell\theta_o - kz)\right\} dz, \tag{15}$$

where the z dependence of θ in the first-order term has been ignored for convenience. For off-axis particles we can write

$$\theta(z) = \Delta\theta \sin \beta_o z, \tag{16}$$

where $\Delta\theta \leq \pi$. Then if we employ the identity

$$e^{j\rho \sin\phi} = \sum_{n=-\infty}^{\infty} J_n(\rho)\, \ell^{jn\phi}, \tag{17}$$

Eq. 15 becomes

$$\Delta v_+ = \sum_{a,b} \int_0^L \kappa v_t J_a\left(\frac{\beta}{k} h(kr)^{\ell}\right) J_b((\ell-1)\Delta\theta)\, \exp -j\{(\beta_o(b+1)-k)z + a(\ell\theta_o - kz)\}\, dz. \tag{18}$$

To lowest order, $J_a = \delta_{ao}$ and resonances appear at

$$k = (b+1)\,\beta_o \tag{19}$$

with their relative amplitudes given by the ratio of the Bessel functions $J_b((\ell-1)\Delta\theta)$. As h increases, subresonances should appear at

$$(a+1)\,k = (b+1)\,\beta_o. \tag{20}$$

Two well-defined subresonances have been observed for particles injected along the axis, where h is quite small, and their spacing is given by (19) with b = 0, 1. Furthermore, if $\Delta\theta$ is taken equal to π for these particles (because their orbits intersect the axis), the relative amplitudes of the observed resonant peaks are given quite closely by the ratio

$$\frac{\Delta I_o}{\Delta I_1} = \left(\frac{\Delta v_{\perp o}}{\Delta v_{\perp 1}}\right)^2 \approx \left(\frac{J_o(2\pi)}{J_1(2\pi)}\right)^2. \tag{21}$$

When the beam was injected off axis, which is equivalent to an increase in h, a complicated fine structure appeared, superimposed on the main peaks. This can be qualitatively identified as the effect of the resonance condition given by Eq. 20. Thus it is apparent that a great deal of information can be extracted from the equations of motion when they are written in the form of Eq. 7. Although the agreement with experiment indicated in this report is mainly qualitative, more exact solutions can be obtained by using iterative techniques.

J. F. Clarke

References

1. K. D. Snelnikov et al, Soviet Phys. – Tech. Phys. 5, 236 (1960A).

2. R. C. Wingerson, Phys. Rev. Letters 6, 446 (1961).

3. E. W. Laing and A. E. Robson, J. Nucl. Energy (Part C. Plasma Physics) 3, 146 (1961).

4. R. C. Wingerson, T. H. Dupree, and D. J. Rose, Phys. Fluids 7, 1475 (1964).

5. R. A. Demirkhanov, Yu. V. Kursanov, D. C. Baratov, and C. V. Klarin, Soviet Phys. – Tech. Phys. 9, 45 (1964).

M. DETERMINING THE ELECTRON DISTRIBUTION FUNCTION FROM SCATTERED LIGHT II*

The electron velocity distribution function in a plasma can be uniquely related to the spectral intensity of photons scattered out of an incident, collimated, monochromatic beam. Thus, in principle, the velocity distribution function can be completely determined. A previously reported initial investigation[1] into the relation between the spectrum and the electron distribution function (including its sensitivity) has been extended and concluded. Details of the work have been presented in an S. M. thesis[2]; only the principal results are given in this report.

The electron velocity distribution function, $f(\underline{\beta})$, where $\underline{\beta}(=\underline{v}/c)$ is the velocity of the electrons, is mapped into the spectral intensity $s(\underline{n}\omega)$ by the operator L_o. $s(\underline{n}\omega)$, the power per unit frequency interval at ω scattered into a unit solid angle in the direction of the unit vector $\underline{n}$, is given by

$$s(\underline{n}\omega) = L_o f(\underline{\beta}). \tag{1}$$

Similarly, the inverse relation is

$$f(\underline{\beta}) = L_o^{-1}\, s(\underline{n}, \omega). \tag{2}$$

The operators L_o and L_o^{-1} have been derived[2] for both relativistic and nonrelativistic cases. Since the relativistic expressions are too complex to be very useful, only the nonrelativistic expressions will be given here:

$$L_o = \frac{3}{8\pi}\,\sigma_T n_e I_o \frac{\omega^2}{\omega_o^3}\left(1-(\underline{n}\cdot\underline{n}_o)^2\right)\int d\underline{\beta}\;\delta(g(\underline{n},\omega,\beta)) \tag{3}$$

and

$$L_o^{-1} = -\frac{12\omega_o^3}{\sigma_T I_o n_e}\int\frac{d\underline{\Omega}_n}{4\pi}\,\frac{(1-\underline{n}\cdot\underline{n}_o)}{(1-(\underline{n}\cdot\underline{E})^2)(1-\underline{n}\cdot\underline{\beta})^3}\,\frac{\partial^2}{\partial\omega^2}\Bigg|_{\frac{\omega}{\omega_o}=\frac{1-\underline{n}_o\cdot\underline{\beta}}{1-\underline{n}\cdot\underline{\beta}}} \tag{4}$$

The notation is the same as that used in a previous report.[1] In L_o^{-1} the integration is over all directions of $\underline{n}$, and the derivative must be evaluated at the given point. Equations 3 and 4 show that the relationship between the distribution function and the spectral intensity of scattered light is unique.

*This work was supported in part by the United States Atomic Energy Commission (Contract AT(30-1)-3221).

Table XI-1. Magnitude, shape functions, and half-widths of various distributions.

f	$\frac{S_m}{n_e r_e^2 I_o \frac{\omega^2}{\omega_o^2} \frac{\sin^2\theta}{\sqrt{2}\,\omega_o\beta_o\sqrt{1-\cos\phi}}}$	y	$\frac{\delta\omega}{\sqrt{2}\,\omega_o\beta_o\sqrt{1-\cos\phi}}$	$\frac{\beta_{avg}}{\beta_o}$	$\frac{(\beta^2)_{avg}}{\beta_o^2}$
$\frac{1}{\pi^{3/2}\beta_o^3}\exp\left[-(\beta/\beta_o)^2\right]$	$\frac{1}{\sqrt{\pi}}$	$\exp\left[-\left(\frac{\omega-\omega_o}{\delta\omega}\right)^2\right]\ln 2$	$\sqrt{\ln 2} = .832$	$\frac{2}{\sqrt{\pi}}$	$\frac{3}{2}$
$\frac{3\exp\left[-(\beta/\beta_o)^4\right]}{4\pi\Gamma\left(\frac{7}{4}\right)\beta_o^3}$	$\frac{3\sqrt{\pi}}{8\Gamma(7/4)}$	$1-\operatorname{erf}\left[\left(\frac{\omega-\omega_o}{\delta\omega}\right)^2 .474\right]$	.688	$\frac{3}{4\Gamma\left(\frac{7}{4}\right)} = .816$	$\frac{3\Gamma\left(\frac{5}{4}\right)}{4\Gamma\left(\frac{7}{4}\right)} = .74$
$\frac{\beta_o/\pi^2}{\left(\beta_o^2+\beta^2\right)^2}$	$\frac{1}{\pi}$	$\frac{1}{1+\left(\frac{\omega-\omega_o}{\delta\omega}\right)^2}$	1	–	–
$\frac{3}{\pi\beta_o^3}\left(1-\frac{\beta}{\beta_o}\right)$	1	$1-\frac{3}{4}\left(\frac{\omega-\omega_o}{\delta\omega}\right)^2+\frac{1}{4}\left(\frac{\omega-\omega_o}{\delta\omega}\right)^3$	1/2	.6	.4
$\frac{1-u(\beta_o)}{\frac{4}{3}\pi\beta_o^3}$	$\frac{3}{4}$	$1-\frac{1}{2}\left(\frac{\omega-\omega_o}{\delta\omega}\right)^2$	$\frac{1}{\sqrt{2}}$	$\frac{3}{4}$	$\frac{3}{5}$
$\frac{15\left(1-(\beta/\beta_o)^2\right)}{8\pi\beta_o^3}$	$\frac{15}{16}$	$1-(2-\sqrt{2})\left(\frac{\omega-\omega_o}{\delta\omega}\right)^2+\left(\frac{2-\sqrt{2}}{2}\right)^2\left(\frac{\omega-\omega_o}{\delta\omega}\right)^4$	.541	$\frac{5}{8}$	$\frac{3}{7}$
$\frac{\delta(\beta-\beta_o)}{4\pi\beta^2}$	$\frac{1}{2}$	$1-u(\omega\pm\delta\omega)$	1	1	1
$\frac{S}{\pi^{3/2}\beta_o^3}\exp\left[-(\beta/\beta_o)^2\right]$ $+\frac{F}{\pi^{3/2}\beta_f^3}\exp\left[-(\beta/\beta_f)^2\right]$	$\frac{S\beta_f+F\beta_o}{\sqrt{\pi}\,\beta_f}$	$\frac{\beta_f\beta_o}{S\beta_f+F\beta_o}\left(\frac{S\exp\left[-\left(\frac{\omega-\omega_o}{\Delta\omega_s}\right)^2\right]}{\Delta\omega_s}+\frac{F\exp\left[-\left(\frac{\omega-\omega_o}{\Delta\omega_f}\right)^2\right]}{\Delta\omega_f}\right)$	–	$\frac{2}{\sqrt{\pi}}\left(S+\frac{\beta_f}{\beta_o}F\right)$	$\frac{3}{2}\left(S+\left(\frac{\beta_f}{\beta_o}\right)^2 F\right)$

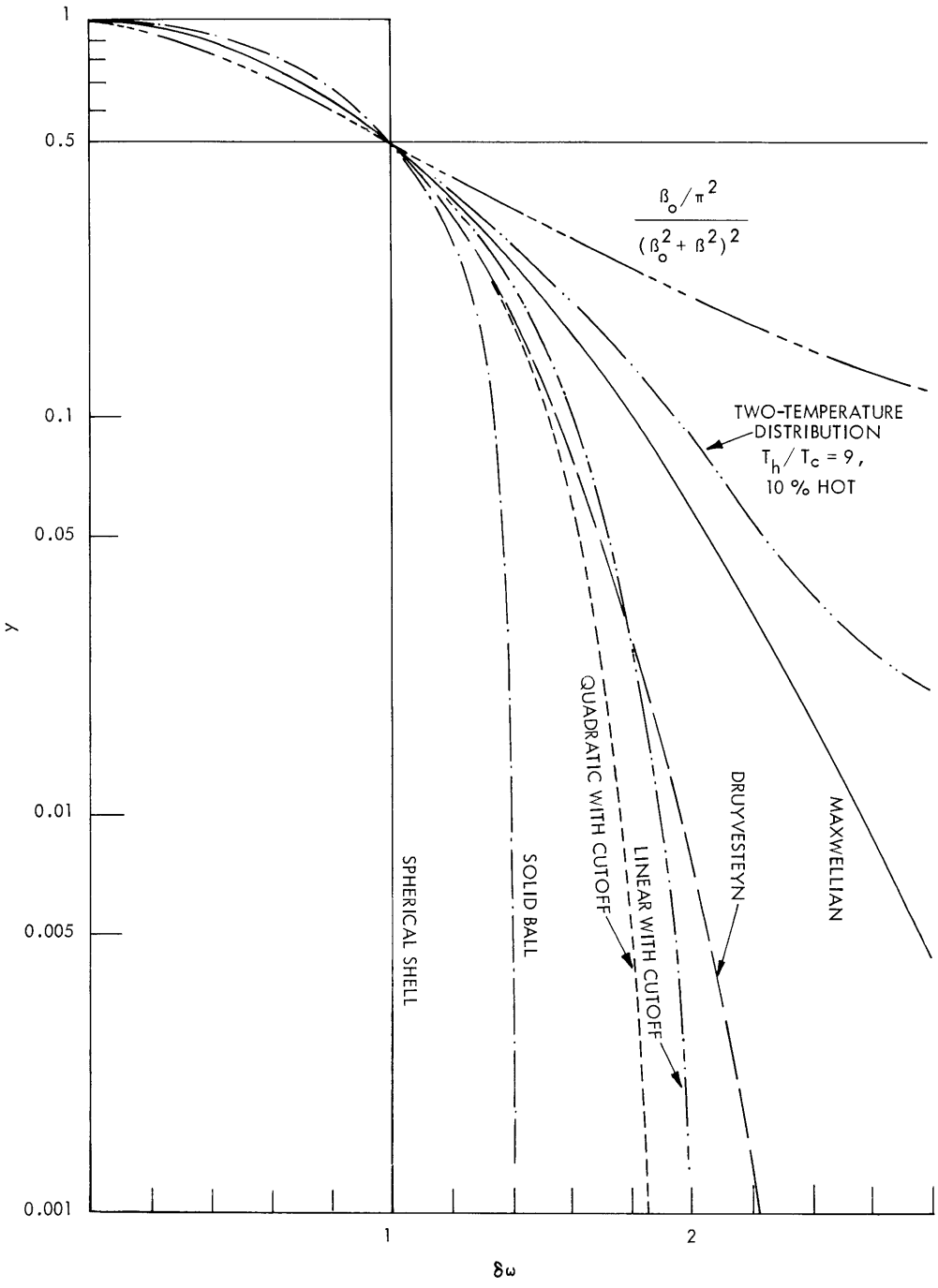

Fig. XI-29. Plot of the shape functions.

From (4) it can be seen that to determine an arbitrary velocity distribution function at a point in velocity space, a great deal of information about the spectral intensity of the scattered light is required. In particular, a specific average, over all directions of scattering, of the second derivative of the spectral intensity (evaluated at a specific frequency which depends on the direction of scattering) is required. In the present simpler experimental arrangements, light is scattered by plasma electrons out of a laser beam and detected in only one or two directions. What is needed in addition to Eq. 2 is a more pragmatic approach, one which would be useful to an experimentalist. Such an approach can be developed by examining Eq. 1.

From (1) it has been shown[1] that the spectrum observed in any particular direction is equivalent to an analysis of the distribution function in one dimension along a specific direction. Thus, one can expect to carry out experimentally only a finite number of one-dimensional density analyses in velocity space of the distribution function. These one-dimensional analyses are useful insofar as some kind of symmetry can be assumed. Even if some kind of symmetry is assumed, the second derivative of the spectrum (a very difficult quantity to determine experimentally) must be measured in order to ascertain the causative distribution function. A method of avoiding such a difficult measurement is to compare the experimental spectrum with spectra calculated by using known distribution functions, that is, to construct a library. A unique method of comparing the experimental and calculated spectra is given below. A rudimentary library calculated from some spherically symmetric distribution functions is illustrated in Fig. XI-29 and the corresponding parameters are listed in Table XI-1.

In order to compare the calculated and experimental spectra, we must note that the shape of the spectrum is the same as the one-dimensional shape of the distribution function and hence the magnitude of the spectrum (corresponding to the electron density) and the width of the spectrum (corresponding to the 1-D velocity spread of the electrons) can be removed as separate factors, leaving only the shape of the spectrum.

This remaining spectral shape is uniquely related only to the one-dimensional distribution function shape. Variations in the two remaining dimensions of the distribution function are indeterminate. The magnitude and width of the spectrum are removed by scaling the plot of the spectrum in such a manner that the ordinate of the maximum is unity, and the abscissa of the half-maximum is unity. The result is a shape function, y. Comparison of the experimental shape functions with the library shape functions (Fig. XI-29) then gives the type of distribution function. The magnitude of the half-width at half-height, $\delta\omega$, gives the average speed and energy (Table XI-1), and the absolute magnitude of the spectral intensity at its maximum, s_m, gives the electron density n_e (Table XI-1).

The accuracy of this analysis depends, of course, on how precisely the experimental spectrum is known. Although the relationship is unique in the one-dimensional sense,

it is well to note that for most distribution functions the relative difference in the resulting spectrum is greatest in the "tail" where the magnitude of the experimental signal is minute, most difficult to measure, and easily obscured by noise. For example, there is little difference between the shape functions of the linearly decreasing and Druyvesteyn distribution functions until the Doppler frequency shift is greater than two half-widths (that is, $2\delta\omega$). Deviations from the commonly assumed Maxwellian distribution can be measured, however, and the average speed and energy can easily be obtained.

T. S. Brown

References

1. T. S. Brown, Determining the electron distribution function from scattered light, Quarterly Progress Report No. 74, Research Laboratory of Electronics, M. I. T., July 15, 1964, pp. 146-149.

2. T. S. Brown, S. M. Thesis, Department of Nuclear Engineering, M. I. T., September 10, 1964.

N. THOMSON SCATTERING DIAGNOSTICS OF A HOLLOW-CATHODE ARC PLASMA*

Preliminary results of an experiment designed to study Thomson scattering of laser radiation as a plasma diagnostic method were reported in Quarterly Progress Report No. 75 (pages 81-84). This work continues and data yielding a much higher signal-to-noise ratio have been obtained. The higher signal to noise was obtained by using an input system of short focal length for the laser radiation which focused a large fraction of the laser output energy into the interaction volume. The use of this system eliminated the possibility of doing the small-angle scattering experiment mentioned in the previous report. It appeared, however, that this would be a very difficult experiment with the present ruby laser for several other reasons. We decided, therefore, to concentrate the effort on obtaining good large-angle scattering data.

The plasma electron temperatures and densities obtained from the present scattering data generally agree well with those obtained from pulsed Langmuir probe measurements performed by M. Lubin. Lubin's measurements are described in Section XI-O. In general, the Thomson scattering data points lie on a Gaussian distribution with departures at certain shifted wavelengths. One of these departures occurs at wavelengths very near the incident laser wavelength. This anomaly was apparently the source of the "low temperature" distribution reported in Quarterly Progress Report No. 75. The reasons for these deviations from a Gaussian distribution are not understood at present.

1. Hollow-Cathode Arc Plasma Source

The hollow-cathode arc facility used for the scattering experiments was not described in any detail in Quarterly Progress Report No. 75. We shall discuss its properties now. The apparatus as viewed looking toward the laser is shown in Fig. XI-30. The cathode is a 3-inch length of 1/8 inch diameter, 0.010-inch wall, tantalum tubing. The anode is a 1-inch I.D., water-cooled hollow structure through which gas may be fed. A low-conductance pumping baffle was installed between the cathode chamber and the scattering chamber with each chamber being separately pumped. This allowed a relatively low background pressure of the order of 10^{-4} torr in the scattering chamber, even with relatively high gas flow rates through the cathode. The anode was grounded with the cathode running at a negative potential. The addition of anode flow seemed to stabilize the arc in this configuration and provide increased electron density. Without the anode gas flow the arc seemed to have difficulty negotiating the pumping baffle. When the baffle was allowed to float electrically it attained a potential near that of the cathode. When it was

*This work was supported in part by the United States Atomic Energy Commission (Contract AT(30-1)-3221).

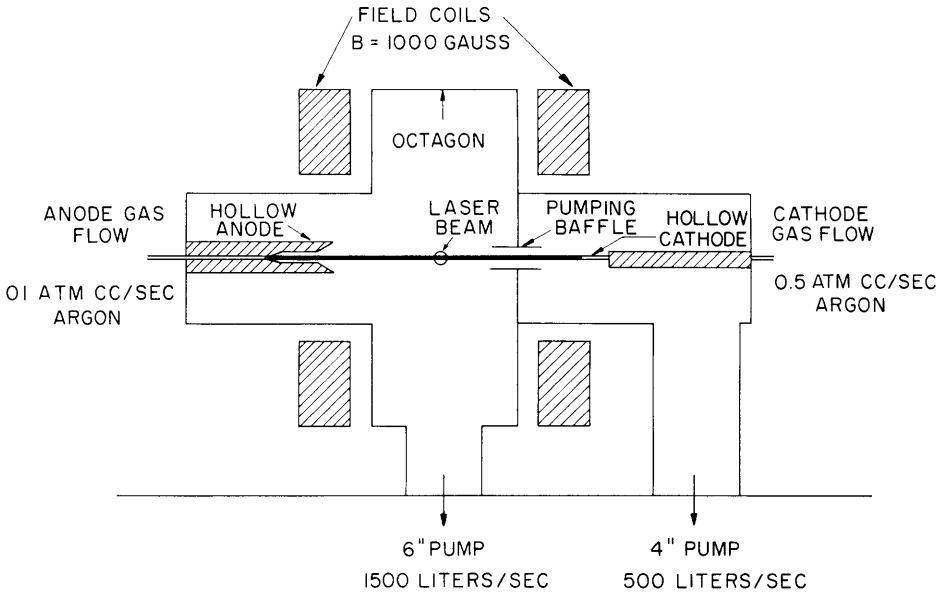

Fig. XI-30. Hollow-cathode arc plasma facility.

grounded approximately 70 per cent of the current went to the baffle, and only 30 per cent to the anode. The arc column in the scattering chamber was very diffuse.

By adding a very small gas flow through the anode (small compared with that through the cathode), the baffle could be made to float at zero potential and thus draw no current when grounded. In this way, the baffle could be eliminated, as far as its effect on the electrical characteristics of the arc are concerned, and thus serve only as a pumping baffle. The arc column in the scattering chamber under these conditions was a well-defined bright column, approximately 1 cm in diameter, with an electron density of approximately $5 \times 10^{13}/cm^3$ at an arc current of 40 amps. The total arc length was 17 inches. The field coils provided a magnetic field of approximately 1000 gauss at the cathode and anode, which were placed at the mirror points, and a field of approximately 500 gauss at the center in the scattering chamber.

Additional flexibility was attained with the introduction of an anode gas feed, in that mixed gas operation could be accomplished. With the cathode running in argon, hydrogen or helium could be introduced through the anode. The result was a relatively pure hydrogen or helium plasma in the scattering chamber, made possible by the strong differential pumping between the two chambers. Of course, some argon was present, but the measured intensities of major argon lines were more than a factor of 20 less than the intensities observed with the arc running in pure argon. The visual effect was quite striking. A bright blue argon arc would disappear into the pumping baffle from the cathode side and emerge as a bright red hydrogen arc in the scattering chamber. The arc would also be run in pure helium and by replacing the tantalum cathode with a

piece of Tungsten-Rhenium alloy tubing of the same dimensions, operation in pure hydrogen was possible.

2. Thomson Scattering Experiment

A schematic view of the scattering apparatus as seen from the cathode end of the arc is shown in Fig. XI-31. The output of the 100-joule ruby laser is focused into the scattering volume by the 50-cm focal length quartz input lens. The focal point for parallel light is at the scattering center, while the focal point for all light leaving the end of the ruby rod is just in front of the entrance to the offset conical-beam dump. This is the advantage of this short focal length system over the old 180-cm focal length system. All light from the laser is focused near the scattering center, while with the old system only the light emitted in the plane-parallel mode from the laser was focused at all, since the laser rod was inside the focal distance of the lens. The offset conical-beam dump was generally of the same type as that used by Thompson[1] in his experiments, except that the cone was offset to eliminate scattering from the necessarily finite-sized tip.

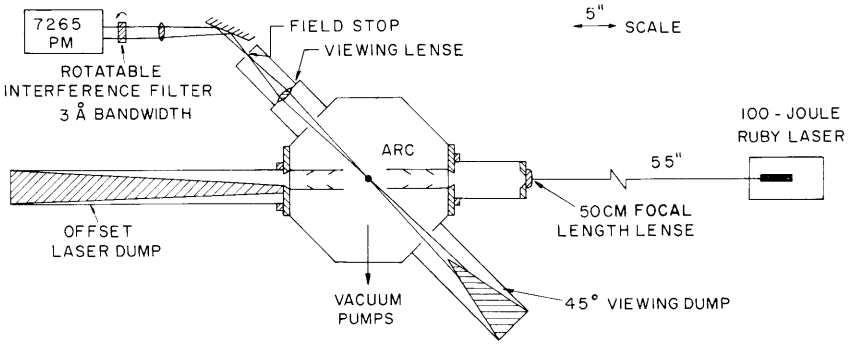

Fig. XI-31. 45° scattering arrangement with 50-cm focal-length lens viewed from cathode end.

Scattering was observed at 45°, the scattering volume being defined by the intersection of the laser beam with the image of the field stop formed by the viewing lens. For the plasmas under study in this device, 45° was a sufficiently large angle so that coherent effects could be neglected (see Quarterly Progress Report No. 75, pp. 81-84). The spectrum of scattered radiation in this case is just the Doppler-broadened spectrum mirroring the electron velocity distribution function in one dimension. After passing through the field stop, the scattered radiation was made parallel by a second lens before passing through the interference filter. The spectrum was scanned by rotating the 3 Å bandwidth interference filter. The radiation was detected by an RCA 7265 photomultiplier with an S-20 photocathode.

Laser light, scattered from the walls of the apparatus, was important only near the

laser line, and disappeared rapidly as the filter was tuned away from the line. The light baffling and collimation was sufficiently good so that this noise was only one-third of the total signal at the laser wavelength. The largest source of noise on the signals was the natural Bremsstrahlung from the plasma. Since the light from the plasma was continuous, this noise could be reduced by using a 150-μsec time constant integrator at the oscilloscope input; 150 μsec was short enough compared with the 1-msec laser pulse duration to preserve the laser pulse shape. The residual noise ultimately limited the magnitude of the smallest observable signal. All data points presented are the result of an overlay of three successive oscilloscope traces taken under the same conditions. The error bars indicate the vertical width of the overlaid traces. The scattered radiation was observed to be fully plane-polarized, as was the laser output. The scattered radiation was synchronous with the input laser radiation. No delayed effects such as those reported by Thompson[2] were observed. Such effects could be produced by raising the neutral background pressure in the scattering chamber by throttling the pump.

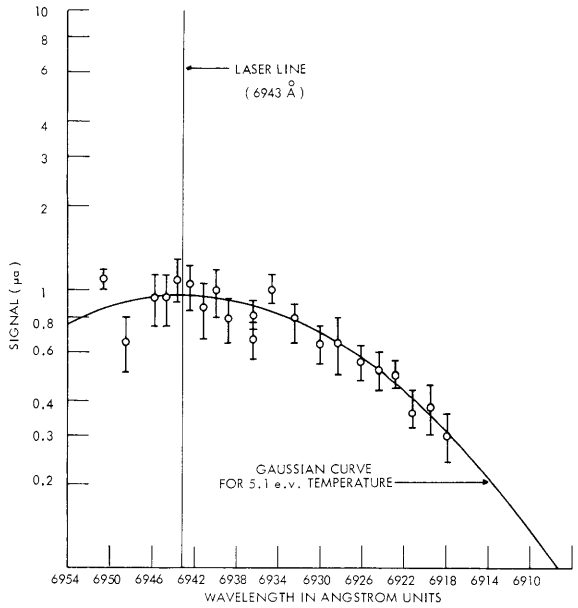

Fig. XI-32. Thomson scattering signal vs wavelength. (Wavelength variation by rotating 6950.5 Å filter.)

Figure XI-32 exhibits some typical data plotted against wavelength, obtained with the arc running in argon. These data were obtained with a 6950.5 Å filter, so that some points are available on both sides of the laser line. A Gaussian curve corresponding to an electron temperature of 5.1 ev is drawn for comparison. Note the departure from the Gaussian, occurring 6-8 angstrom units either side of the laser line.

Figure XI-33 exhibits the same data as in Fig. XI-32 replotted against electron energy. The energy of the electron responsible for the scattering at a given shifted wavelength is proportional to the wavelength shift squared. A Gaussian electron velocity distribution is represented by a straight line on this plot.

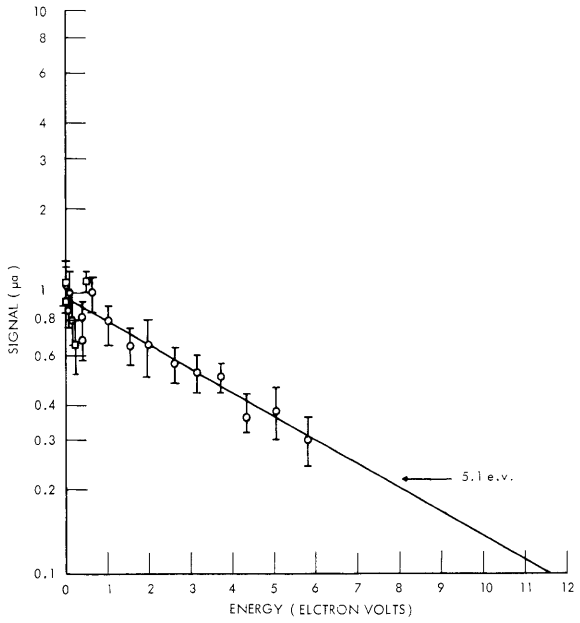

Fig. XI-33. Thomson scattering signal vs electron energy.
(Wavelength variation by rotating 6950.5 Å filter.)
Points from long-wavelength side.
Points from short-wavelength side.

Data obtained with a 6938 Å filter and with the arc running under the same conditions as for Figs. XI-32 and XI-33 are shown in Fig. XI-34. Note, again, the apparent departures from the Gaussian line drawn on the figure. The reasons for these departures from a Gaussian distribution are not at present understood. They are possibly due to actual deviations of the electron velocity distribution from Maxwellian. More likely, they are due to effects from electronically excited atoms or ions such as Raman scattering, or Rayleigh scattering from nearby emission lines.

Agreement with the probe data of M. Lubin, described in Section XI-O, is generally good. For an arc current of 40 amps in argon, he obtains electron temperatures in the range of 6.5-8.5 ev. We obtain temperatures in the range 4.5-5.5 ev, somewhat lower. This discrepancy is in the direction expected. Lubin finds electron densities in the range $4.5\text{-}7.5 \times 10^{13}$. Calibrating the system by using Rayleigh scattering from a known density of nitrogen, we obtain densities of 4×10^{13} which can be considered good

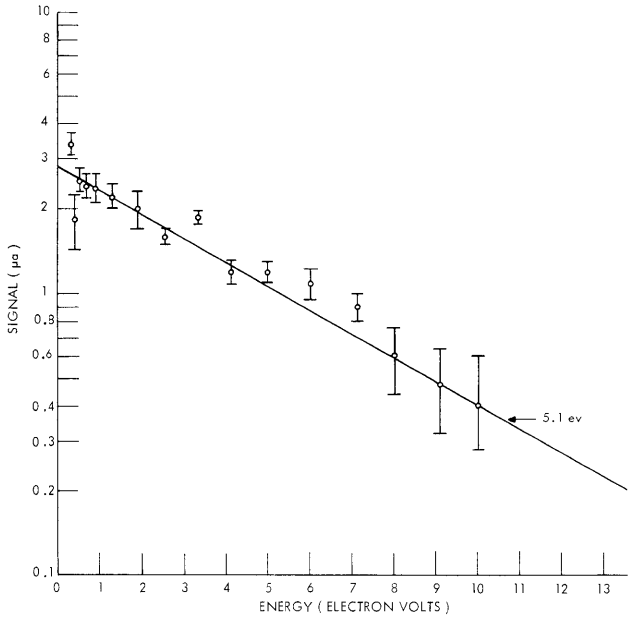

Fig. XI-34. Thomson scattering signal vs electron energy. (Wavelength variation by rotating 6938.2 Å filter.)

agreement, since the uncertainties involved in obtaining electron densities from probe measurements are large.

The discrepancy between the electron temperature obtained from the probe data and the scattering data can probably be understood in the following way. The scattering system is sensitive to electron velocities only in the plane of scattering, which in this case is perpendicular to the magnetic field, so that with this system we can measure a perpendicular temperature $T_{\perp}$. The probe, however, collects electrons from an oval-shaped region, with the long dimension of the oval along the field. Thus the probe is primarily sensitive to parallel electron velocities, $T_{\parallel}$, with some contribution from $T_{\perp}$. Since the electrons gain their energy from the electric field of the arc, which is parallel to the magnetic field, perpendicular energy is obtained only through relaxation by collision. At the electron densities and temperatures under consideration here the mean-free path for an electron is only slightly smaller than the anode-cathode distance. Thus it might be expected that $T_{\perp}$ would be less than $T_{\parallel}$.

Further evidence for this reasoning can be obtained by examining the electron temperature as a function of magnetic field strength for both the probe and scattering measurements. The probe data shown in Fig. XI-41 in Section XI-O (Lubin's report) exhibit a tendency of constant or slightly decreasing measured electron temperature with increasing magnetic field. On the other hand, the Thomson scattering data, shown in Fig. XI-35 exhibit a tendency of increasing the electron temperature with increasing

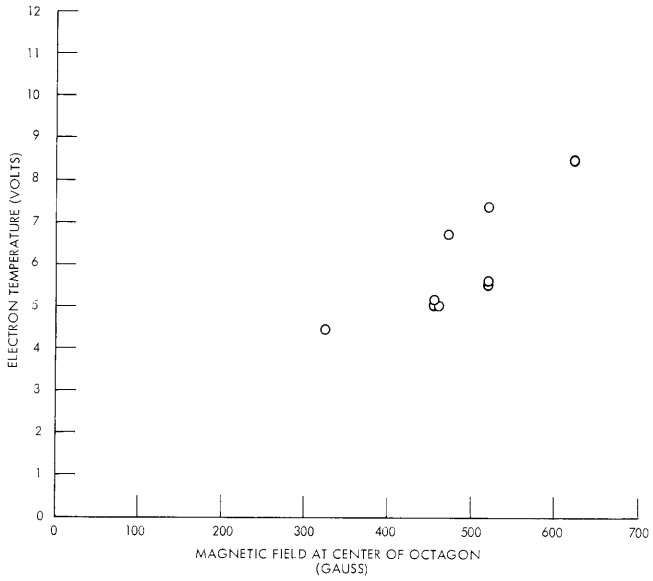

Fig. XI-35. Thomson scattering data. (Electron temperature vs magnetic field strength.)

magnetic field. This would be expected on the basis of the present discussion. The diameter of the arc column is observed to decrease as the magnetic field is increased, with the result that a higher ion density is exhibited in Fig. XI-40 in Section XI-O. A higher ion density reduces the time for relaxation of parallel energy to perpendicular energy, thereby yielding closer agreement between $T_{\perp}$ and $T_{\parallel}$.

Scattering data were also obtained with the arc running in hydrogen and helium but no unusual effects were observed.

E. T. Gerry

References

1. E. Thompson and G. Fiocco, Quarterly Progress Report No. 69, Research Laboratory of Electronics, M.I.T., April 15, 1963, pp. 74-80.

2. E. Thompson, Quarterly Progress Report No. 75, Research Laboratory of Electronics, M.I.T., October 15, 1964, pp. 68-80.

O. PULSED LANGMUIR PROBE MEASUREMENTS ON A HOLLOW-CATHODE DISCHARGE*

Langmuir probe measurements have been made on the hollow-cathode discharge described in Section XI-N.

In order to avoid melting probes in the high-density plasma, characteristics were obtained by a transient technique by using a simple passive circuit. The circuit is diagrammed in Fig. XI-36. The probe, when idle, is at floating potential. When the

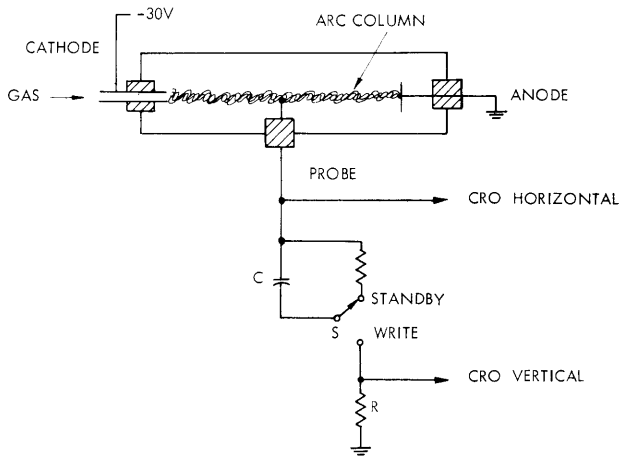

Fig. XI-36. Circuit concept.

switch is thrown to the write position, the probe is momentarily placed at anode potential, and the plasma electron current charges the capacitor C through R. The probe voltage and the voltage across R are displayed as the horizontal and vertical deflections, respectively, of an oscilloscope trace. When the capacitor is charged, the probe is once again at floating potential and draws no current. Ion current at potentials more negative than floating potential is measured by the usual DC methods.

Typical records of probe characteristics and their logarithmic rectifications are shown in Fig. XI-37. Electron temperature and ion density are calculated according to the formulas of Bohm, Burhop, and Massey.[2]

*This work was supported in part by the United States Atomic Energy Commission (Contract AT(30-1)-3221).

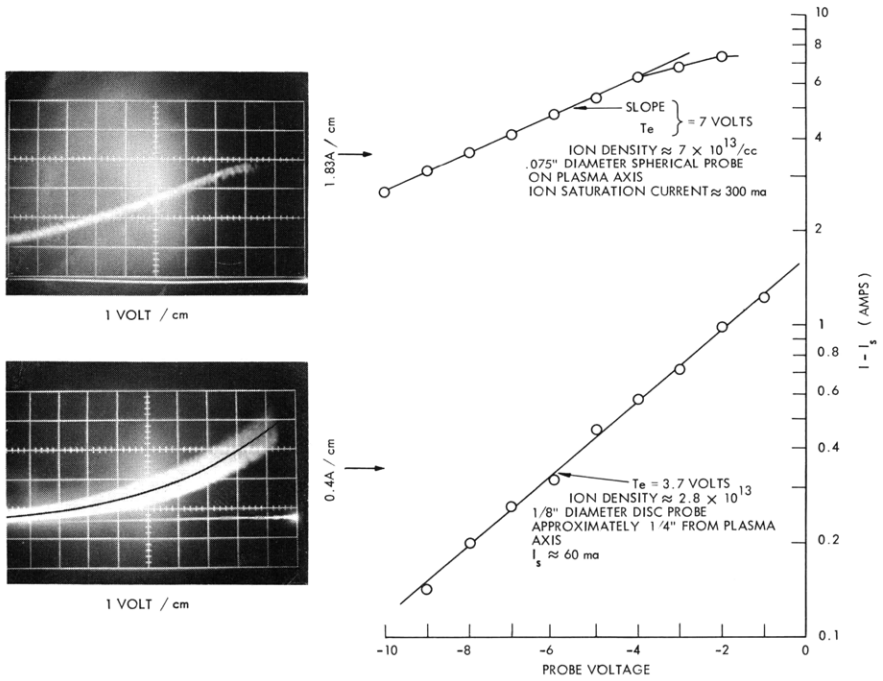

Fig. XI-37. Records of probe characteristics and their logarithmic rectifications.

Plots of electron temperature and ion density against arc current and axial magnetic field measured at various times with various probes are shown in Figs. XI-38 through XI-41. Measurements were made on the axis of the plasma, in the position from which Thomson scattering was observed by E. T. Gerry. All probe measurements were made on argon plasmas.

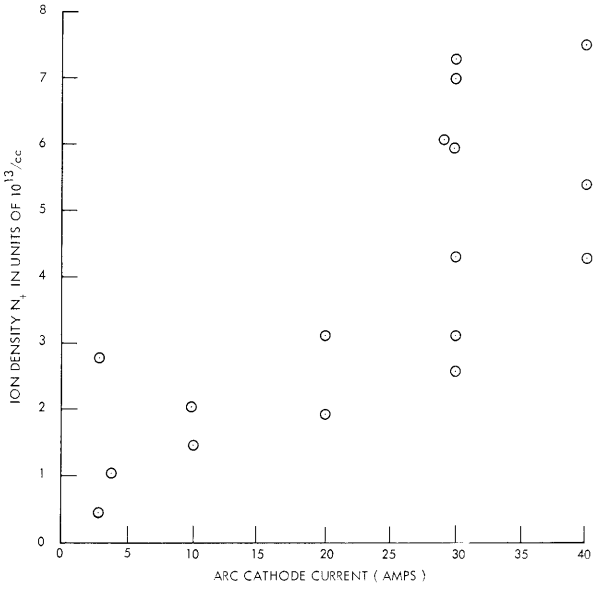

Fig. XI-38. Ion density vs arc current. Magnetic field, 450 gauss; probe centered in the arc.

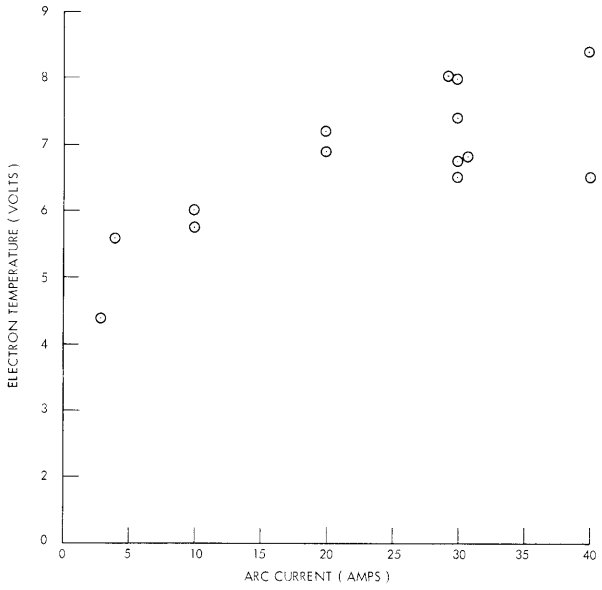

Fig. XI-39. Electron temperature vs arc current. Magnetic field, 450 gauss; probe centered in plasma.

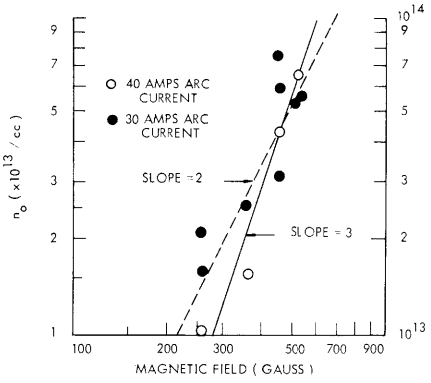

Fig. XI-40. Ion density vs magnetic field.

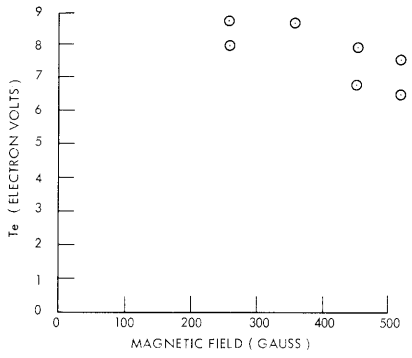

Fig. XI-41. Electron temperature vs magnetic field (30 amps arc current).

Table XI-2 gives a summary of results obtained by using probes of various shapes and sizes at one of Gerry's standard conditions. The comparison of these data with the Thomson scattering data has been reported in Section XI-N.

Table XI-2. Summary of results.

Gas Argon

Cathode flow 0.62 atm-cc/sec

Anode flow 0.175 atm-cc/sec

Magnetic Field 454 gauss

	Arc Current (amps)			
	10	20	30	40
Ion Density (units of 10^{13}/cc)	1.5-2	2-3.3	3-7	4.5-7.5
kTe (electron volts)	6	7	6.5-8	6.5-8.5

M. D. Lubin

References

1. E. T. Gerry, Research Laboratory of Electronics, M.I.T., Quarterly Progress Report No. 75, October 15, 1964, p. 81.

2. D. Bohm, E. H. S. Burhop, and H. S. W. Massey, The Use of Probes for Plasma Exploration in Strong Magnetic Fields. The Characteristics of Electrical Discharges in Magnetic Fields, edited by A. Guthrie and R. K. Wakerling (McGraw-Hill Book Company, New York, 1949), Chapter II.

P. ELECTRON TRANSPORT IN THREE-COMPONENT PLASMAS

1. Introduction

The purpose of this report is to present a technique for analysis of electron transport phenomena in three-component plasmas.

Transport phenomena in nonuniform gaseous mixtures have been analyzed by others.[1-4] In particular, Chapman and Cowling[4] have developed a formalism for the solution of a set of Boltzmann equations through a series of successive approximations. This formalism has been successfully used in the field of gas dynamics, under the assumption that, to a first approximation, all components of the mixture have the same temperature.

A modified Chapman-Cowling approach is used here to determine the electron distribution function and current and heat flux in a three-component plasma in which the electron temperature is different from the ion and neutral-particle temperatures. A similar method has recently been presented by Stachanov and Stepanov.[3] These authors, however, treated the charged-particle collisions by means of the small-angle Landau approximation and used a hard-sphere model for electron-neutral collisions. As well as removing these restrictions on the collision integrals, the present analysis yields the electron transport parameters in a form that is more amenable to physical interpretation.

This report has two main parts. First, a perturbation method similar to Chapman and Cowling's will be used to solve the Boltzmann equation for electrons. Then, the practicality of the perturbation method will be illustrated through its application to both reference Lorentz plasmas and a three-component plasma.

2. Perturbation Solution of the Boltzmann Equation

a. The Boltzmann Equations

The Boltzmann equations in a steady state, three-component plasma consisting of electrons (e), ions (i), and neutrals (n), may be written

$$\overline{v}_\alpha \cdot \nabla_r f_\alpha + \frac{q_\alpha \overline{E}}{m_\alpha} \cdot \nabla_v f_\alpha = \sum_\beta J_{\alpha\beta}(f_\alpha, f_\beta); \qquad \alpha, \beta = e, i, n, \tag{1}$$

where $J_{\alpha\beta}$ is the collision integral for collisions between species α and β. This integral may be written in Boltzmann form as

$$J_{\alpha\beta}(f_\alpha, f_\beta) \equiv \iiint (f'_\alpha f'_\beta - f_\alpha f_\beta)\, g_{\alpha\beta} b \frac{db}{dx}\, dx d\epsilon dv_\beta \tag{2}$$

where $g_{\alpha\beta} = |\overline{v}_\alpha - \overline{v}_\beta|$; b is the impact parameter; x and ϵ are the polar and azimuthal angles describing the rotation (in the center of mass coordinates) of the relative velocity vector during the collision; and $f'_\alpha = f_\alpha(\overline{r}, \overline{v}'_\alpha)$, with $\overline{v}'_\alpha$ the velocity before the collision. In writing Eq. 2 for like-particle collisions ($J_{\alpha\alpha}$), the second subscript is omitted. This eliminates confusion concerning the variables of integration. Further details concerning the geometry and derivation of Eq. 2 may be found in Chapman and Cowling.[5]

b. Small m_e/m_β Approximation

The system of Eqs. 1 represents, in general, a set of three coupled, nonlinear, six-dimensional equations for the distribution functions $f_\alpha(\overline{r}, \overline{v}_\alpha)$; $\alpha = e, i, n$. This system of equations may be greatly simplified by utilizing the fact that the mass ratio m_e/m_β (β=i, n) is small and noting that

$$J_{e\beta}(f_e, f_\beta) = J_{e\beta}[f_e, n_\beta \delta(\overline{v}_\beta)] + 0(m_e/m_\beta); \quad \beta = i, n, \tag{3}$$

where n_β is the density of species β, and $\delta(x)$ is the Dirac delta function. Physically, Eq. 3 implies that in the Boltzmann equation for electrons, the heavy particles may, to a good approximation, be regarded as stationary. The result is that the electron equation is decoupled from those for the heavy particles (in velocity space). The rest of this part of the report is devoted to the solution of the Boltzmann equation for electrons.

c. Linearized Boltzmann Equation

In seeking a solution for the electron distribution function $f_e(\overline{r}, \overline{v}_e)$, it is convenient to define a perturbation function, $\phi_e(\overline{r}, \overline{v}_e)$, by means of the equation

$$f_e(\overline{r}, \overline{v}_e) = f_e^o(\overline{r}, \overline{v}_e)\,[1+\phi_e(\overline{r}, \overline{v}_e)], \tag{4}$$

where

$$f_e^o(\overline{r}, \overline{v}_e) \equiv n_e(m_e/2\pi kT_e)^{3/2} \exp\left(-m_e v_e^2/2kT_e\right) \tag{5}$$

$$n_e = \int f_e \, d\underline{v}_e; \quad \frac{3}{2} n_e kT_e = \int \left(m_e v_e^2/2\right) f_e \, dv_e \tag{6}$$

Thus, the perturbation ϕ_e must satisfy the conditions

$$\int f_e^o \phi_e \, d\underline{v}_e = 0; \quad \int v_e^2 f_e^o \phi_e \, d\underline{v}_e = 0. \tag{7}$$

With these definitions and conditions the linearized Boltzmann equation for electrons is

$$\frac{1}{n_e} f_e^o \left\{ \overline{v}_e \cdot \left(\frac{\nabla_r P_e}{P_e} + \frac{eE}{kT_e} \right) + \left(u_e^2 - \frac{5}{2} \right) \overline{v}_e \cdot \frac{\nabla_r T_e}{T_e} \right\} = -n_e I_e(\phi_e) - n_i I_{ei}(\phi_e) - n_n I_{en}(\phi_e), \tag{8}$$

where

$$\overline{u}_e = (m_e/2kT_e)^{1/2} \overline{v}_e \tag{9}$$

and the linear integral operators I_e and $I_{e\beta}$ are defined as

$$I_e[F_e(\overline{v}_e)] \equiv \frac{1}{n_e^2} \iiint f_e^o f^o (F_e + F - F_e' - F') \, g_e b \, db d\epsilon d\underline{v} \tag{10}$$

$$I_{e\beta}[F_e(\overline{v}_e)] \equiv \frac{1}{n_e} \iint f_e^o (F_e - F_e') \, v_e b \, db d\epsilon. \tag{11}$$

In definitions (10) and (11), $F_e(\overline{v}_e)$ may be a scalar or a vector function of $\overline{v}_e$, and $f^o = f_e^o(\overline{r}, \overline{v})$, $F = F_e(\overline{v})$, $F_e' = F_e(\overline{v}_e')$, $F' = F_e(\overline{v}')$, and $g_e = |\overline{v}_e - v|$.

d. Solution of the Linearized Boltzmann Equation

The general solution of Eq. 8 is

$$\phi_e = -\frac{1}{n_e}(2kT_e/m_e)^{1/2} \left\{ \overline{A}_e(\overline{u}_e) \cdot \left(\frac{\nabla P_e}{P_e} + \frac{e\overline{E}}{kT_e} \right) + \overline{B}_e(\overline{u}_e) \cdot \frac{\nabla T_e}{T_e} \right\} + C_1 m_e + C_2 m_e v_e^2/2, \tag{12}$$

where $\overline{A}_e$, $\overline{B}_e$ are vector functions of the electron velocity and C_1, C_2 are arbitrary constants. The first two terms on the right-hand side of Eq. 12 represent the particular solutions for each of the driving terms in Eq. 8, while the last two terms represent the homogeneous solution.

Substitution of Eq. 12 in Eq. 8 yields

$$f_e^o \overline{u}_e = n_e I_e(\overline{A}_e) + n_i I_{ei}(\overline{A}_e) + n_n I_{en}(\overline{A}_e) \tag{13}$$

$$\left(u_e^2 - \frac{5}{2} \right) f_e^o \overline{u}_e = n_e I_e(\overline{B}_e) + n_i I_{ei}(\overline{B}_e) + n_n I_{en}(\overline{B}_e). \tag{14}$$

Since Eqs. 13 and 14 contain only $\overline{u}_e$ as an independent variable, $\overline{A}_e$ and $\overline{B}_e$ must be of the form

$$\overline{A}_e(\overline{u}_e) = A_e(u_e)\,\overline{u}_e/u_e; \quad \overline{B}_e(\overline{u}_e) = B_e(u_e)\,\overline{u}_e/u_e, \tag{15}$$

where $A_e(u_e)$ and $B_e(u_e)$ are scalar functions of the magnitude of $\overline{u}_e$.

From Eqs. 7-15 we find that

$$C_1 = C_2 = 0, \tag{16}$$

$$I_{e\beta}(\overline{G}) = \frac{1}{n_e} f_e^o v_e \sigma_{e\beta}(v_e)\,\overline{G}; \quad \overline{G} = \overline{A}_e, \overline{B}_e, \tag{17}$$

where

$$\sigma_{e\beta}(v_e) \equiv 2\pi \int (1 - \cos x)\, b\, db \tag{18}$$

is the momentum transfer cross section.

The meaning of Eqs. 12-18 is that the problem of determining the electron distribution function $f_e(\overline{r}, \overline{v}_e)$ is reduced to that of finding two scalar functions $A_e(u_e)$ and $B_e(u_e)$ that are solutions of Eqs. 13 and 14, respectively. These equations can be solved exactly only for a Lorentz plasma (see below). In the general case of a three-component plasma one resorts to approximation techniques which will be discussed below.

e. Sonine Polynomial Expansions for $A_e(u_e)$ and $B_e(u_e)$

For a general three-component plasma, it is expedient to expand the scalar functions $A_e(u_e)$ and $B_e(u_e)$ into series of Sonine polynomials[7] of order 3/2:

$$A_e(u_e)/u_e = \sum_{n=0}^{\infty} a_n S_n^{3/2}\left(u_e^2\right); \quad B_e(u_e)/u_e = \sum_{n=0}^{\infty} b_n S_n^{3/2}\left(u_e^2\right), \tag{19}$$

where a_n, b_n are expansion coefficients, and $S_n^{3/2}(x)$ is a Sonine polynomial of order 3/2. Substitution of these expansions in Eqs. 13 and 14, dot-multiplication of the result by $S_m^{3/2}\left(u_e^2\right)\overline{u}_e$, and integration over velocity space yields two infinite sets of linear algebraic equations of the form

$$\sum_{n=0}^{\infty} \alpha_{mn} a_n = \beta_m$$

$$m = 0, 1, \ldots \infty, \tag{20}$$

$$\sum_{n=0}^{\infty} \alpha_{mn} b_n = \gamma_m,$$

where

$$\alpha_{mn} \equiv \alpha_{mn}^{ee} + \alpha_{mn}^{ei} + \alpha_{mn}^{en};$$

$$\alpha_{mn}^{ee} \equiv \int S_m^{3/2}\left(u_e^2\right)\overline{u}_e \cdot I_e\left[S_n^{3/2}\left(u_e^2\right)\overline{u}_e\right] d\underline{v}_e;$$

$$\alpha_{mn}^{e\beta} \equiv \frac{n_\beta}{n_e} \int S_m^{3/2}\left(u_e^2\right)\overline{u}_e \cdot I_{e\beta}\left[S_n^{3/2}\left(u_e^2\right)\overline{u}_e\right] d\underline{v}_e; \tag{21}$$

$$\beta_m \equiv \frac{1}{n_e} \int S_m^{3/2}\left(u_e^2\right) u_e^2 f_e^o \, d\underline{v}_e = \frac{3}{2}\delta_{mo},$$

$$\gamma_m \equiv \frac{1}{n_e} \int S_m^{3/2}\left(u_e^2\right) u_e^2\left(u_e^2 - \frac{5}{2}\right) f_e^o \, d\underline{v}_e = -\frac{15}{4}\delta_{m1}.$$

Thus, the problem of solving Eqs. 13 and 14 for the scalar functions $A_e(u_e)$ and $B_e(u_e)$ is reduced to that of solving the two infinite sets of Eqs. 20 for the Sonine expansion coefficients a_n and b_n. Approximate solutions to any desired degree of accuracy may be obtained by truncating the Sonine expansions after N terms and solving the resulting 2N equations. The matrix elements α_{mn}, in principle, may be determined once the collision laws are specified. Specifically, the quantities α_{mn}^{ee} are special cases of a general set of like-particle collision integrals which have been tabulated by Chapman and Cowling,[6] while $\alpha_{mn}^{e\beta}$ can be evaluated by using Eq. 17 for the operator $I_{e\beta}$. It can also be shown that $\alpha_{mn} = \alpha_{nm}$.[6]

f. Electron Current and Heat Flux

The electron current, $\overline{J}_e$, and the electron heat flux, $\overline{q}_e$, are given by

$$\overline{J}_e \equiv e \int \overline{v}_e f_e \, d\underline{v}_e = -\mu_e\left\{\nabla P_e + e n_e \overline{E} + k_e^T n_e \nabla kT_e\right\} \tag{22}$$

$$q_e \equiv \int \overline{v}_e \frac{m_e v_e^2}{2} f_e \, d\underline{v}_e = \frac{J_e}{e}\frac{5}{2}kT_e + \frac{\overline{J}_e}{e}k_e^T kT_e - \mathcal{K}_e \nabla T_e, \tag{23}$$

where

$$\mu_e \equiv \frac{2e}{3n_e^2 m_e} \int f_e^o u_e A_e(u_e) \, d\underline{v}_e \qquad \text{(electron mobility)} \tag{24}$$

$$k_e^T \equiv \frac{2e}{3n_e^2 m_e \mu_e} \int f_e^o u_e B_e(u_e) \, d\underline{v}_e \qquad \text{(thermal diffusion ratio)} \tag{25}$$

$$\mathcal{K}_e \equiv \frac{\mu_e n_e k^2 T_e}{e}\left\{\frac{2e}{3n_e^2 m_e \mu_e}\int f_e^o u_e^3 B_e(u_e)\, d\underline{v}_e - k_e^T\left(\frac{5}{2}+k_e^T\right)\right\} \qquad \text{(thermal conductivity)} \tag{26}$$

The last term in (22) is the "thermal diffusion" term of Chapman and Cowling and other authors. The first term on the right-hand side of (23) represents enthalpy transport, the second term is the "diffusion thermo-effect," an energy transport mechanism related to the thermal diffusion mechanism in Eq. 22, and the third term accounts for thermal conduction. The definitions of the transport coefficients μ_e, k_e^T, and $\mathcal{K}_e$ are consistent with the usual definitions of these quantities.

In terms of the Sonine expansion coefficients Eqs. 24-26 become

$$\mu_e = \frac{ea_o}{n_e m_e}; \quad k_e^T = \frac{b_o}{a_o}; \quad \mathcal{K}_e = -\frac{5}{2}\frac{k^2 T_e}{m_e}\left(b_1 + \frac{2}{5}k_e^T b_o\right). \tag{27}$$

3. Applications of the Perturbation Method

a. Lorentz Plasmas

For a Lorentz plasma Eqs. 13 and 14 may be solved exactly. Hence the Lorentz plasma provides a convenient reference case for comparisons. Specifically, for a Lorentz plasma consisting of electrons and heavy particles of species β only, the perturbation function and transport coefficients are

$$\phi_e = \lambda_{e\beta}\left\{\frac{\nabla P_e}{P_e} + \frac{e\overline{\overline{E}}}{kT_e} + \left(u_e^2 - \frac{5}{2}\right)\frac{\nabla T_e}{T_e}\right\}\cdot\frac{\overline{u}_e}{u_e} \tag{28}$$

$$\mu_e = \frac{e}{P_e}\int \frac{v_e^2}{3\nu_{e\beta}} f_e^o\, dv_e$$

$$k_e^T = \frac{e}{\mu_e P_e}\int \frac{v_e^2}{3\nu_{e\beta}}\left(\frac{m_e v_e^2}{2kT_e} - \frac{5}{2}\right) f_e^o\, d\underline{v}_e \tag{29}$$

$$\mathcal{K}_e = \frac{\mu_e k P_e}{e}\left\{\frac{e}{\mu_e P_e}\int \frac{v_e^2}{3\nu_{e\beta}}\left(\frac{m_e v_e^2}{2kT_e}\right)^2 f_e^o\, d\underline{v}_e - \left(\frac{5}{2}+k_e^T\right)^2\right\},$$

where $\lambda_{e\beta}(v_e) = 1/n_\beta \sigma_{e\beta}(v_e)$ is the electron mean-free path, and $\nu_{e\beta}(v_e) = v_e/\lambda_{e\beta}(v_e)$ is is the e-β collision frequency. Note that the perturbation ϕ_e is small (compared with unity) when the fractional changes in the electron pressure and temperature and in the plasma potential are small over one mean-free path.

Table XI-2. Special values of the transport coefficients for Lorentz plasmas.

Heavy-Particle Species	Neutrals	Neutrals	Ions
Collision Law	ν_{en} = const	λ_{en} = const	Coulomb
μ_e	$\frac{e}{m_e \nu_{en}}$	$\frac{e\lambda_{en} v_a}{3kT_e}$	$128\left(\frac{\pi}{2}\right)^{1/2} \frac{\epsilon_o^2 (kT_e)^{3/2}}{n_i e^3 m_e^{1/2} \ln \Lambda}$
k_e^T	0	-1/2	+3/2
$\mathcal{K}_e$	$\frac{5}{2} \frac{n_e k^2 T_e}{m_e \nu_{en}}$	$\frac{2}{3} n_e k \lambda_{en} v_a$	$512\left(\frac{\pi}{2}\right)^{1/2} \frac{n_e k \epsilon_o^2 (kT_e)^{5/2}}{n_i e^4 m_e^{1/2} \ln \Lambda}$
Note: v_a = electron mean speed = $(8kT_e/\pi m_e)^{1/2}$; ln Λ = coulomb logarithm.			

Shown in Table XI-2 are values of the transport coefficients obtained from Eqs. 29 for three Lorentz plasmas of special interest: (i) the heavy particles are neutrals and ν_{en} = constant; (ii) the heavy particles are neutrals and λ_{en} = constant; (iii) the heavy particles are ions. A Lorentz plasma of the third type is a purely hypothetical case, since the neglect of e-e collisions as compared with e-i collisions requires that $n_e \ll n_i$, a condition that is never achieved in practice. Note that the values in Table XI-2 are in agreement with similar results derived by other techniques.

The transport coefficients for a Lorentz plasma can also be computed by means of the Sonine polynomial expansion technique. For example, for a Lorentz plasma in which the heavy particles are neutrals and λ_{en} = constant, these coefficients for N = 1, 2,

Table XI-3. Transport coefficients for Lorentz plasma with constant λ_{en}.

Terms in Sonine Expansion	$\mu_e/(\mu_e)_{exact}$	$k_e^T/\left(k_e^T\right)_{exact}$	$\mathcal{K}_e/(\mathcal{K}_e)_{exact}$
N = 1	0.88	0	0
N = 2	0.95	0.77	0.85
N = 3	0.98	0.90	0.93

and 3 can be readily evaluated and compared with the exact values given in Table XI-2. This comparison reveals (Table XI-3) that retention of three terms in each of the Sonine expansions is sufficient to yield all three transport coefficients correctly within 10 per cent.

b. Three-Component Plasmas with Constant ν_{en}.

Another illustration of the application of the Sonine polynomial expansion technique is the computation of the transport coefficients for a three-component plasma with ν_{en} = constant and $n_e \approx n_i$. If three terms are again retained in each of the expansions, the matrix elements a_{mn} can be readily evaluated, and they lead to the following set of equations:

$$\begin{bmatrix} 1 + 1.50\nu_{en}/\nu_{ei} & 1.50 & 1.87 \\ 1.50 & 4.66 + 3.75\nu_{en}/\nu_{ei} & 5.37 \\ 1.87 & 5.37 & 10.7 + 13.1\nu_{en}/\nu_{ei} \end{bmatrix} \begin{bmatrix} a_o \\ a_1 \\ a_2 \end{bmatrix} = \begin{bmatrix} 1.50 n_e/\nu_{ei} \\ 0 \\ 0 \end{bmatrix} \tag{30}$$

$$\begin{bmatrix} 1 + 1.50\nu_{en}/\nu_{ei} & 1.50 & 1.87 \\ 1.50 & 4.66 + 3.75\nu_{en}/\nu_{ei} & 5.37 \\ 1.87 & 5.37 & 10.7 + 13.1\nu_{en}/\nu_{ei} \end{bmatrix} \begin{bmatrix} b_o \\ b_1 \\ b_2 \end{bmatrix} = \begin{bmatrix} 0 \\ -3.75 n_e/\nu_{ei} \\ 0 \end{bmatrix} \tag{31}$$

Here, $\nu_{ei} \equiv \dfrac{e^4 \ln \Lambda v_a n_i}{4\pi\epsilon_o^2 (2kT_e)^2}$ is the effective electron-ion collision frequency.

Solution of Eqs. 30-31 yields a_n, b_n which in turn can be used in Eqs. 27 to calculate the transport coefficients. The results of the calculation are given in Table XI-4.

The second column of Table XI-4 gives the values of the coefficients in the Lorentz limit $\nu_{ei} \ll \nu_{en}$, denoted by the superscript "o"; they are identical to the corresponding values in Table XI-2. The reason is that the Sonine expansion technique with $N \geq 2$ yields an exact solution for the Lorentz plasma with constant ν_{en}.

The third column of Table XI-4 gives the values of the electron transport coefficients in the fully ionized limit $\nu_{ei} \gg \nu_{en}$. They are denoted by the superscript "∞", and are in excellent agreement with results reported by Chapman and Cowling[3] and by Samokhin.[8] By comparing the values for μ_e^∞, $\left(k_e^T\right)^\infty$, and $\mathcal{K}_e^\infty$ with the corresponding values in Table XI-2 for a hypothetical e-i Lorentz plasma, the importance of electron-electron collisions is deduced. The effect of e-e collisions is to reduce each of the transport coefficients (in the fully ionized limit) approximately from one-fourth to one-half the value obtained in the absence of e-e collisions.

Table XI-4. Transport coefficients in a three-component plasma.

	Lorentz Limit ($\nu_{ei} \ll \nu_{en}$)	Fully Ionized Limit ($\nu_{ei} \gg \nu_{en}$)	General Expression
μ_e	$\mu_e^o = \dfrac{e}{m_e \nu_{en}}$	$\mu_e^\infty = 0.57 \times 128 \left(\dfrac{\pi}{2}\right)^{1/2} \dfrac{\epsilon_o^2 (kT_e)^{3/2}}{e^3 n_i m_e^{1/2} \ln \Lambda}$	$\mu_e = \dfrac{\mu_e^o \mu_e^\infty}{\mu_e^o + \mu_e^\infty} h_\mu(\mu)$
k_e^T	$\left(k_e^T\right)^o = 0$	$\left(k_e^T\right)^\infty = 0.71$	$k_e^T = \left(k_e^T\right)^\infty h_k(\mu)$
$\mathcal{K}_e$	$\mathcal{K}_e^o = \dfrac{5}{2} \dfrac{n_e k^2 T_e}{m_e \nu_{en}}$	$\mathcal{K}_e^\infty = 0.23 \times 512 \left(\dfrac{\pi}{2}\right)^{1/2} \dfrac{k\epsilon_o^2 (kT_e)^{5/2}}{e^4 m_e^{1/2} \ln \Lambda}$	$\mathcal{K}_e = \dfrac{\mathcal{K}_e^o \mathcal{K}_e^\infty}{\mathcal{K}_e^o + \mathcal{K}_e^\infty} h_{\mathcal{K}}(\mu)$

The fourth column of Table XI-4 lists the values of the coefficients for values of ν_{ei}/ν_{en} lying between the Lorentz and fully ionized limits. The functions $h_\mu(\mu)$, $h_k(\mu)$, and $h_{\mathcal{K}}(\mu)$ are given by

$$h_\mu(\mu) = \frac{1.00 + 7.00\mu + 9.67\mu^2 + 3.67\mu^3}{1.00 + 7.93\mu + 10.9\mu^2 + 3.67\mu^3}$$

$$h_k(\mu) = \frac{1.00\mu + 0.89\mu^2}{0.24 + 1.46\mu + 0.89\mu^2} \tag{32}$$

$$h_{\mathcal{K}}(\mu) = \frac{1.00 + 11.9\mu + 45.1\mu^2 + 73.2\mu^3 + 52.0\mu^4 + 13.5\mu^5}{1.00 + 13.9\mu + 62.0\mu^2 + 95.0\mu^3 + 65.9\mu^4 + 13.5\mu^5},$$

where

$$\mu \equiv \frac{\mu_e^o}{\mu_e^\infty} = 0.34 \frac{\nu_{ei}}{\nu_{en}}.$$

These functions are plotted in Fig. XI-42.

From Fig. XI-42 it is apparent that the function $h_\mu(\mu)$ is nearly unity for all values of μ ($0 \leq \mu \leq \infty$). This implies that, to a good approximation, the contributions to the electron mobility from electron-neutral and from electron-charged particle collisions may be added in parallel. Similar conclusions apply to the contributions to the thermal conductivity of the electrons.

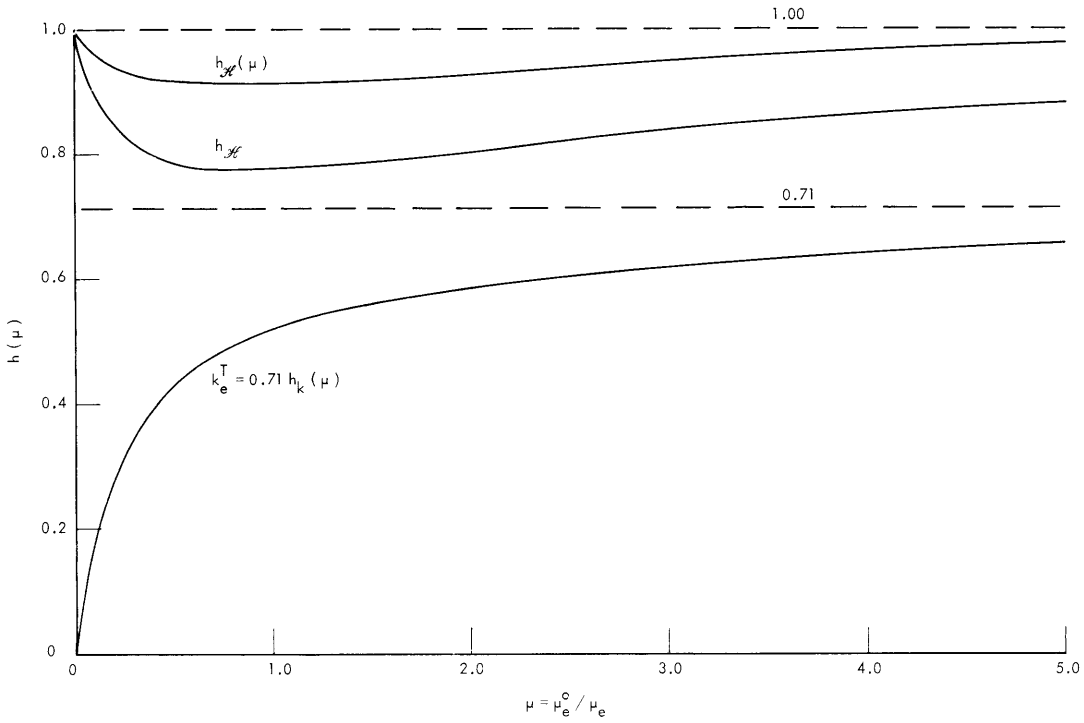

Fig. XI-42. Plots of h(μ) functions against μ.

4. Conclusions

The modified Chapman-Cowling approach presented in this report provides a useful tool for the analysis of three-component plasmas. The method yields both a quantitative description of the electron-particle and energy-transport mechanisms and an analytical expression for the electron distribution function.

D. R. Wilkins, E. P. Gyftopoulos

References

1. H. Grad, Communs. Pure Appl. Math. 2, 324 (1949).

2. J. O. Hirshfelder, C. F. Curtiss, and R. B. Bird, Molecular Theory of Gases and Liquids (John Wiley and Sons, Inc., New York, 1954).

3. I. P. Stachanov and R. S. Stepanov, Soviet Phys. – Tech. Phys. 9, 315 (1964).

4. S. Chapman and T. G. Cowling, The Mathematical Theory of Nonuniform Gases (Cambridge University Press, London, 1961).

5. Ibid, p. 65.

6. Ibid, pp. 85-88; 161.

7. Ibid, p. 124.

8. M. V. Samokhin, Soviet Phys. – Tech. Phys. 8, 498 (1963).

Q. PROBLEMS IN THE THEORY OF OPTIMAL CONTROL OF NONLINEAR SYSTEMS

The existence of solutions to certain optimal control problems has been studied for a multi-input, multi-output nonlinear system that is realizable, and is representable in terms of an input-output functional series of the form

$$\underline{y}(t) = \sum_{j=0}^{\infty} \sum_{i=1}^{i_{j,r}} \int_0^{t-t_o} \cdots \int \underline{h}_{j,i}(\sigma_1, \sigma_2, \ldots, \sigma_j)\, C_i(\underline{u}; \sigma_1, \sigma_2, \ldots, \sigma_j)\, d\sigma_1 d\sigma_2 \ldots d\sigma_j \tag{1}$$

which is an extension of the system representation of Chesler[1] to multi-output case. The optimal control problem in this formulation is to find the input vector $\underline{u}(t) \in U$, $t_o \leq t \leq t_1$, which is such that it satisfies the system and the boundary conditions

$$\underline{\eta} = \sum_{j=0}^{\infty} \sum_{i=1}^{i_{j,r}} \int_0^{t_1-t_o} \cdots \int \underline{h}_{j,i}(\sigma_1, \sigma_2, \ldots, \sigma_j)\, C_i(\underline{u}; \sigma_1, \sigma_2, \ldots, \sigma_j)\, d\sigma_1 d\sigma_2 \ldots d\sigma_j \tag{2}$$

and minimizes the cost functional

$$\mathcal{J}(\underline{u}) = \int_{t_o}^{t_1} \mathcal{L} \left[\underline{u}(t), \sum_{j=0}^{\infty} \sum_{i=0}^{i_{j,r}} \int_0^{t-t_o} \cdots \int \underline{h}_{j,i}(\sigma_1, \sigma_2, \ldots, \sigma_j) \cdot C_i(\underline{u}; \sigma_1, \sigma_2, \ldots, \sigma_j)\, d\sigma_1 d\sigma_2 \ldots d\sigma_j \right] dt, \tag{3}$$

where U is the specified subset of the input space, the n-vector $\underline{\eta}$ is the desired terminal value of the output, the n-vector $\underline{h}_{j,i}(\sigma_1, \sigma_2, \ldots, \sigma_j)$ is the i^{th} component of the j^{th}-order kernel of the nonlinear system, and $C_i(\underline{u}; \sigma_1, \sigma_2, \ldots, \sigma_j)$ is the i^{th} possible j-tuple product of the components of the input vector $\underline{u}(t)$, each factor in the product having σ_1, σ_2, ..., or σ_j as its argument.

We find the set V of the inputs that satisfy Eq. 2, and determine the set $W = V \cap U$. The element $\underline{u}^* \in W$ that minimizes the cost functional, Eq. 3, will then be the optimal input that is sought. If the set V is empty or the sets V and U are disjoint, that is, if the set W is empty, we conclude that no input exists that can perform the prescribed task. If W is nonempty and compact, we ascertain the existence of the optimal input. If W contains only a single element or the element $\underline{u}^* \in W$ that minimizes Eq. 3 is unique, we say that the optimal control problem has a unique solution.

In obtaining the set V, the potentialness of the system operator of Eq. 2 is necessary. The conditions that the kernels $\underline{h}_{j,i}$ must satisfy in order for the system operator to be potential, as well as the potential of the operator, have been found. It has also been found that the set V, if it is not empty, is compact.

The application of the theory to systems that can be represented with only a few terms of the series is now being studied. For these systems, the possibility of developing a computational technique of obtaining the optimal input with respect to some practical cost functionals will be investigated by using the present formulation.

S. H. Kyong

References

1. D. A. Chesler, Nonlinear Systems with Gaussian Inputs, Technical Report 366, Research Laboratory of Electronics, M. I. T., Cambridge, Mass., February 15, 1960.

2. M. M. Vainberg, Variational Methods for the Study of Nonlinear Operators, (Holden-Day, Inc., San Francisco, 1964).